Hindawi
Geofluids
Volume 2022, Article ID 3744053, 26 pages
https://doi.org/10.1155/2022/3744053

Research Article

Study on the Deformation and Stability of Proppant Column in High-Conductivity Channel Fracturing

Ming Wang,[1] **Feng Zhang**,[2,3] **and Hanxiang Wang**[2]

[1]*Shandong Institute of Petrochemical Technology, Dongying, Shandong 257001, China*
[2]*China University of Petroleum (East China), Qingdao, Shandong 266580, China*
[3]*Shengli Oil Field Petroleum Engineering Technology Research Institute, Sinopec, Dongying, Shandong 257000, China*

Correspondence should be addressed to Ming Wang; wang_ming_001@163.com

Received 5 July 2021; Revised 21 January 2022; Accepted 13 April 2022; Published 14 July 2022

Academic Editor: Hetang Wang

The nonlinear constitutive model of the proppant column was established through laboratory experiments on the stability of the proppant column. Based on reservoir geomechanics and the finite element method, a fracture-proppant column interaction model was established for high-conductivity channel fracturing. The effects of in situ stress, reservoir rock elastic parameters, and spatial distribution characteristics of the proppant column on the closure deformation of the high-conductivity fracture channel and the stability of the proppant column were studied. The higher the in situ stress, the higher the contact stress on the rock plate; the lower the height and the larger the diameter of the proppant column, the more prone to deformation and breakage, while the more the effective support decreases with the increase of the in situ stress. Under the condition of constant in situ stress, with the increase of the reservoir elastic modulus, the relative axial displacement of the two slabs decreases gradually, the effective propping ratio of fractures increases, and the reservoir elastic modulus has little effect on the stability of the proppant column. The effective propping ratio decreases with the increase of the proppant column diameter, increases with the increase of the proppant column height, and increases with the increase of the ratio of the reservoir elastic modulus to in situ stress. When the proppant column diameter (proppant column spacing) is less than 3 m, the effective propped fracture ratio increases significantly. Through the above research, the optimal proppant cluster diameter was finally optimized.

1. Introduction

Channel fracturing was first proposed by Gillard et al. [1] in 2010, and its process mainly consists of three parts: multicluster perforation process, fracturing fluid-blending fiber process, and pulse-pumping process. The sand carrier fluid and the displacement fluid were injected into the formation alternately at a certain time ratio, so that there was no proppant between the adjacent two stages. After the fracturing fluid was gouged and flowed back, the proppant cluster formed an unevenly laid proppant column to support the fracture and formed a high-conductivity channel between the adjacent two proppant columns. In channel fracturing, fibers are added to the fracturing fluid to alter proppant rheology, preventing slug dispersion during migration and settlement, and reducing proppant settlement rates, enabling the formation of an ideal proppant cluster in the fracture. As a new type of hydraulic fracturing stimulation technology, high diversion channel-fracturing technology has achieved remarkable results in field application, which not only reduces the cost of fracturing operation but also greatly increases the production. Abroad, for example, the Talinskoe field in Siberia has seen a 51% increase in well production after channel fracturing [2–9]. After channel fracturing in the Burgos Basin in Mexico, initial gas well production increased by 32%, and half-year cumulative gas production increased by 19% [10]. Early production in the Qarun field in the Western Desert of Egypt was increased by 89% after channel fracturing [11]. At present, this technology has been widely used in the Shengli oilfield, Sichuan Basin tight gas reservoirs, and Ordos Basin tight oil and gas reservoirs and achieved good results. For example, after channel fracturing in tight oil and gas reservoirs in the Ordos Basin, China, oil well production is 2.4 times that of

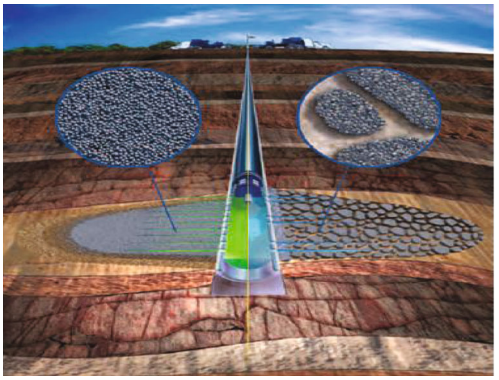

Figure 1: Schematic diagram of proppant placement for conventional hydraulic fracturing (left) and high-speed channel fracturing (right) [1].

Table 1: Value table of experimental factors.

Factors	Values						
Height of proppant columns (mm)	6	8	10	—	—	—	—
Number of proppant columns	5	7	9	—	—	—	—
Closure pressure (MPa)	0.9	6.9	13.8	20.7	27.6	34.5	41.4

conventional fracturing, and gas well production is 4-5 times that of conventional fracturing [12–18]. Therefore, channel-fracturing technology has a broad application prospect in unconventional oil and gas development.

Fractures are supported by dispersed proppant clumps (or columns) that form low-drag flow paths for fluid flow. Compared to conventional fracturing techniques, high-conductivity channel fracturing overcomes the limitations of fluid flow confined to a porous medium, breaks the design philosophy of evenly distributed proppant, and provides higher fracture conductivity (as shown in Figure 1).

The mechanics characteristic of the proppant column is a major factor affecting the law of channel-fracturing fracture closure, the current characteristics of the channel-fracturing proppant column fracture mechanics study is less, the scholars did not delve into the constitutive relation of the fracturing proppant fracture column, most of the proppant elastomer column was regarded as a line, and this is the blank area of the channel-fracturing study.

Many scholars have conducted a large number of laboratory experiments and theoretical studies on the mechanical characteristics and fracture conductivity of the proppant column in channel fracturing. Nguyen et al. [19] conducted fracture conductivity tests for channel fracturing by placing several small cylindrical proppant columns on rock plates based on the APIRP61 fracture conductivity testing standards. The results showed that when the proppant particles were well consolidated, the effective fracture permeability of channel fracturing increased by 1.5 to 2.5 orders of magnitude in comparison with that of conventional fracturing. In 2016, Yan et al. [20, 21] assumed the proppant column as a cylindrical linear elastomer and established a fracture width model considering the deformation and embedding of the proppant column when deducing the channel compression fracture width model. In 2016, Hou et al. [22] also considered the deformation of the proppant column when deducing the fracture width model and calculated the deformation amount of the proppant column through the deformation theory of the proppant. Xu et al. [23], Qu et al. [24], and Wen et al. [25] used the FCS-100 flowmeter to simulate the conductivity of the channel fracture under different sand concentrations, fiber mass fractions, and

Table 2: Experimental groups.

Experimental groups	Height (mm)	Number of columns
1	10	9
2	10	7
3	10	5
4	8	9
5	8	7
6	8	5
7	6	9
8	6	7
9	6	5

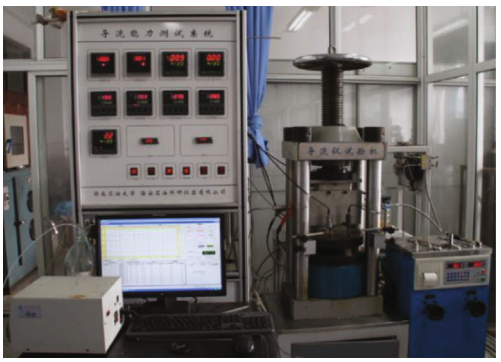

Figure 2: Fracture conductivity testing and analysis system.

Table 3: Experimental groups.

Mineral type	Quartz	Feldspar	Sodium feldspar	Calcite	Silicon carbide	Hematite
Content (%)	92	5	1	2	—	—

proppant column diameters (10~32.8 mm), but they did not study the deformation and failure rule of the proppant column. Zhang [26] took into account the influence of proppant embedding, the axial deformation of the proppant column, and its arrangement and derived an analytical model for the fracture width and conductivity of channel fracturing. Zhang and Hou [27] took the axial deformation of the proppant column into consideration and regarded the proppant clusters formed in the high-speed channel-fracturing fractures as the seepage zone. Based on the Darcy-Brinkman equation, a mathematical model of high conductivity of the high-speed channel-fracturing fractures was established. Zheng et al. [28] obtained the expression of the fracture width based on the Hertz contact theory and proppant embedding theory and then obtained the final conductivity calculation formula. Moghadasi et al. [29] suggested that the utilization of nanosilica particles during hydraulic fracturing could reduce the fines migration and improve the production performance. Guo and Liu [30], based on the interaction between a single proppant particle and rock, and considering the viscoelastic creep effect of rock, established models of long-term conductivity of the conventional fracture and short-term conductivity of the channel fracture. These fracture conductivity models all assume that the proppant column is an elastomer with a certain elastic modulus, ignoring the nonlinear stress-strain characteristics of the proppant column and the nonuniform variation of the fracture width at the open channel. Meyer et al. [31] regarded the deformation of the fracture wall as elastic deformation. Considering the different structural forms of the proppant column in the fracture, an analytical fracture width model was established based on the Hertz contact theory in elastic half space, and the expression of fracture permeability was derived by using Darcy's law and equivalent seepage resistance principle. Hou et al. [32] used Meyer's method for reference to establish the variation model of the proppant column fracture width in channel fracturing. These two models take into account the elastic deformation characteristics of the fracture wall, but the proppant column is still treated as a rigid body.

In this work, the influences of in situ stress, reservoir rock elastic parameters, and proppant column spatial distribution characteristics on the closure deformation of the high-conductivity fracturing channel and the stability of the support column are studied.

2. Deformation Test of Proppant Column in High-Conductivity Channel Fracturing

2.1. Experimental Scheme. Our target is to explore the effects of the proppant column height, arrangement spacing (proppant column number), and closure stress on the deformation of the proppant column. Using the experiments, we measure the destruction of the proppant column shape, axial displacement, radial displacement, and stress-strain characteristics of the proppant column at the stage of compaction and loading pressure. During high-conductivity channel fracturing, the

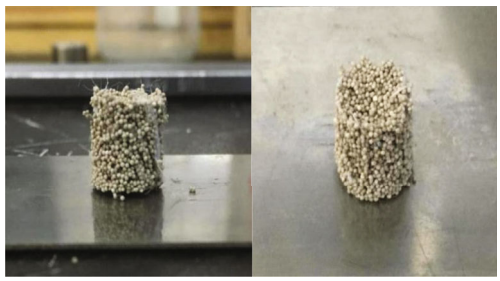

Figure 3: Visual observation of proppant shape.

Figure 4: Test platform installation.

Figure 5: Proppant column after experiment.

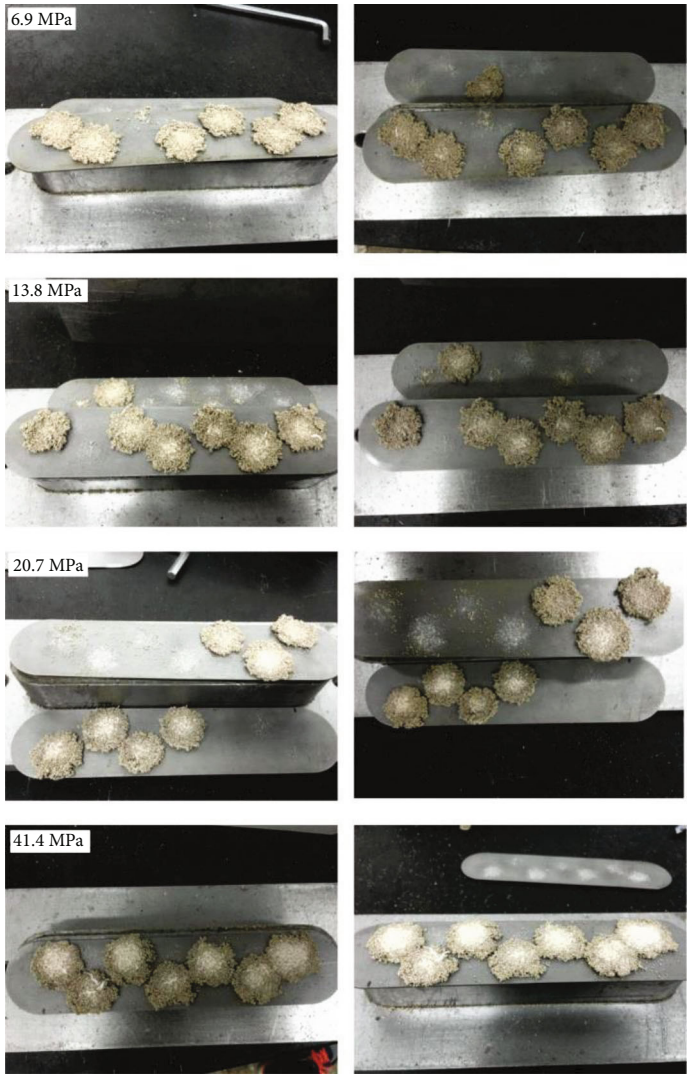

Figure 6: Deformation shape of proppant column.

support columns form a cylindrical shape in the cracks one by one, and the height of the support columns describes the width of the cracks. The closing stress of the cracks is applied to the support columns along the axial direction to describe the deformation behavior of the support columns accurately. The values of each factor are shown in Table 1.

The three proppant column heights and the three proppant column numbers in Table 1 were combined to design a total of nine sets of experiments, and seven closure pressures were arranged for each set of experiments. The specific experimental groups are shown in Table 2.

2.2. Experimental Equipment and Sample Preparation

2.2.1. Experimental Equipment and Sample Preparation. In this experiment, the API standard fracture conductivity test and analysis system was used to conduct simulation experiments. The maximum closure pressure that the equipment could bear was 120 MPa, which could meet the requirements of the experimental design (as shown in Figure 2).

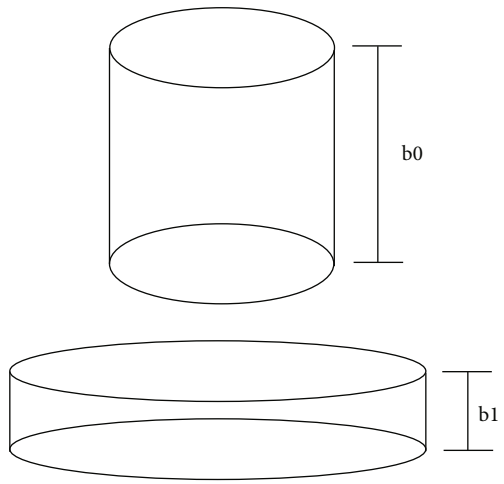

Figure 7: Schematic diagram of proppant stress pattern.

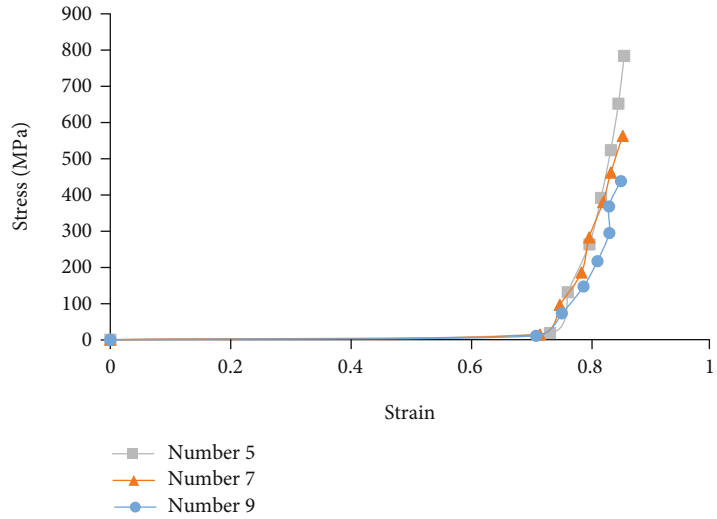

Figure 8: Stress-strain curve of proppant column height (initial proppant column height: 10 mm).

2.2.2. Sample Preparation. The proppant column material used in this experiment is the 40/70-mesh CARBO proppant. Before the experiment, XRD was used to test the mineral composition of the proppant. The specific results are shown in Table 3.

The proppant column produced in this experiment should be approximately cylindrical, the appearance of each proppant column should be basically the same, and it is not easy to collapse and loose and can effectively gather proppant particles. The specific production steps are as follows:

(1) First, weigh 33 g of the selected CARBO proppant material, then weigh the fibers according to the ratio of 4‰ and put them into the beaker

(2) Before adding glue, use hands or a glass rod to break up the fibers in the beaker as much as possible and thoroughly mix them in the proppant particles to prevent the fibers from agglomerating when the glue is added later

(3) Slowly add glue to the beaker while stirring continuously with a glass rod until the proppant particles, fibers, and glue in the beaker are thoroughly mixed and solidified to form a viscous proppant group

(4) Put the proppant cluster into a particular metal model (inner diameter 10 mm, height 1 cm) and fill the model with the proppant cluster through mechanical compaction

(5) Take out the formed proppant column. Put the proppant column into a heating furnace, heat it at 60°C for one hour, and then place it at room temperature for half an hour to obtain a consolidated proppant column (Figure 3).

2.3. Experimental Steps. In this experiment, after the guide chamber is assembled as required, the guide chamber is installed on the test platform to ensure the level of the platform. The guide chamber is correctly placed in the center of the platform, and the pressure testing machine is manually rotated to make the upper part of the test machine just contact the guide chamber (as shown in Figure 4).

(1) *Preparation*: two displacement meters are installed on the diversion chamber.

(2) *Experimental stage*: the pressure pump is used to pressurize the diversion chamber, and the pressure is set for 1 min under the specified pressure to reach a stable state.

(3) *Measurement phase*: write down the values of the two displacement meters, calculate the average value as the total axial displacement, and calculate the converted displacement of the proppant column according to the elastic modulus of the diversion chamber and rock sample. The variation of the crack width is recorded during the experiment using the device's axial displacement sensor. It is expected that the deformation of the instrument is negligible.

As can be seen from Figure 5, under the action of axial pressure, the proppant column spreads evenly along the radial circumference, forming an approximately circular wafer-shaped column. The deformation shapes of the proppant column under different closing pressure are shown in Figure 6. Note that during the experiment, we assume the proppant particle-fiber mixture is well cemented and ignore the effect of drag and carrying on the outermost particles of the support column during the flowback of the fracturing fluid. The stability of the support column during the actual fracturing process may be worse than that during the experiment. The accurate study accounting for these effects is the subject of future studies.

2.4. Nonlinear Constitutive Model of Proppant Column. In this experiment, the proppant deformation is described as shown in Figure 7.

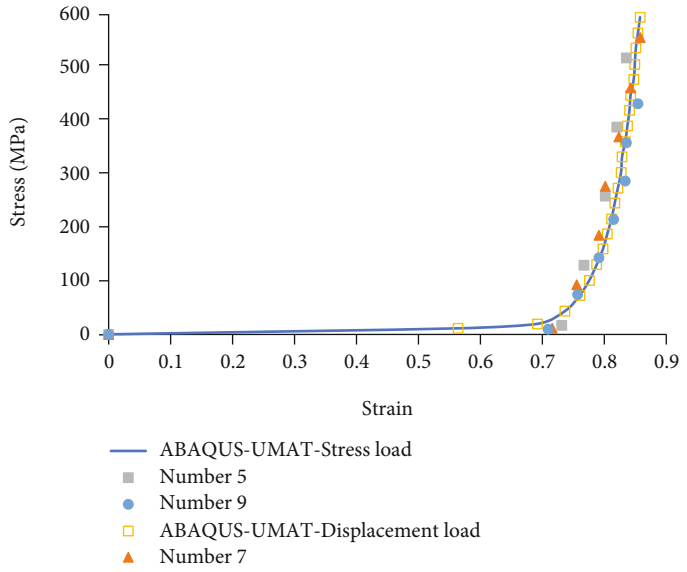

Figure 9: Results of numerical verification (initial height of proppant column: 10 mm).

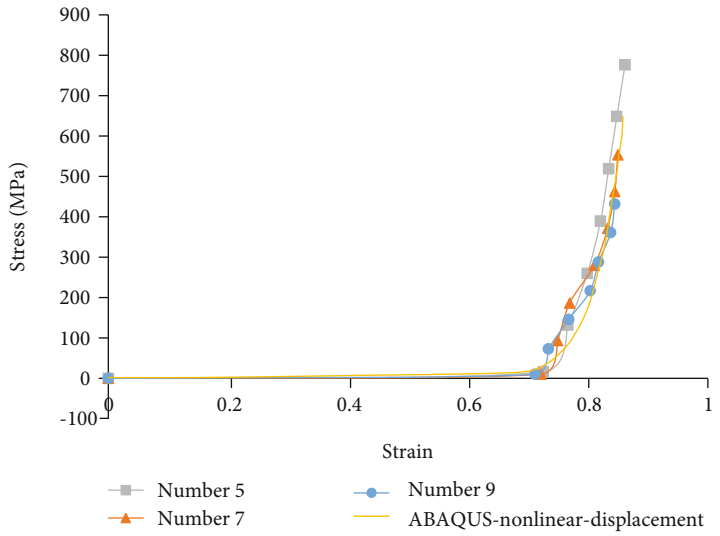

Figure 10: Results of numerical verification (initial height of proppant column: 8 mm).

When the initial height is 10 mm and the number of proppant columns is different, the experimental results are shown in Figure 8.

A nonlinear constitutive model is proposed to describe the experimental results. The form of the constitutive model is as follows:

$$\sigma = E\varepsilon + (K\varepsilon)^n, \tag{1}$$

where E is the equivalent modulus of elasticity, K is the Hardening coefficient, and n is the Sclerosing index.

Nonlinear fitting was used to determine the constants of each material. Figure 9 exhibits the results of numerical verification. The y-axis of this figure is the contact stress caused by the stress concentration. When the initial height of the proppant column was 10 mm, the results of numerical simulation are in good agreement with the experimental results. Therefore, this constitutive model was further used to calculate the numerical results of a proppant column with an initial height of 8 mm. By comparison with the experimental results, the results that are shown in Figure 10 can be obtained. Our model works well for the proppant columns having different heights.

3. Establishment of the Model of Fracturing Crack-Proppant Column Interaction in High-Conductivity Channel

3.1. Model of Fracturing Crack-Proppant Column Interaction in High-Conductivity Channel

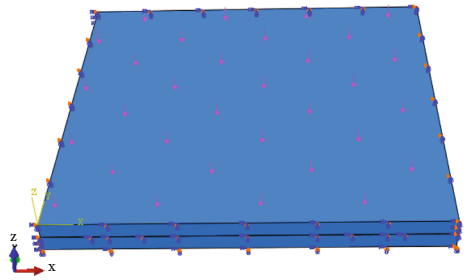

Figure 11: Finite element model of fracturing crack-proppant column interaction in high-conductivity channel.

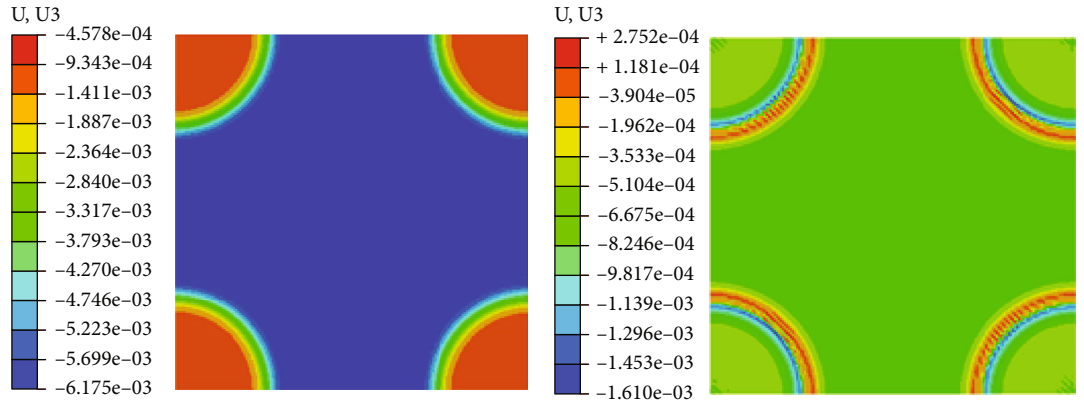

(a) (b)

Figure 12: Displacement cloud images of Z direction of the upper slab (a) and lower slab (b).

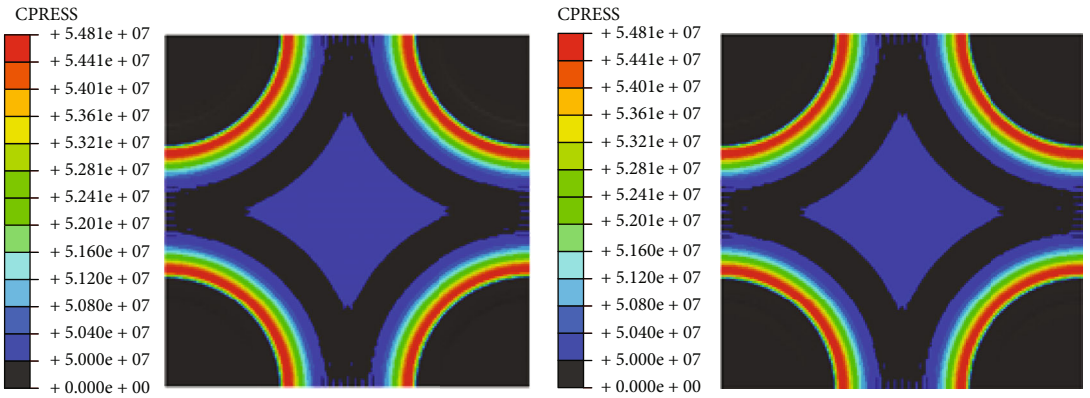

(a) (b)

Figure 13: Contact stress cloud images of upper slab (a) and lower slab (b).

3.1.1. Physical Model of Fracturing Crack-Proppant Column Interaction in High-Conductivity Channel. In this section, based on the parameters of Well A20, a physical model of the fracturing crack-proppant column interaction in the high-conductivity channel was established. The effective fracture length of the well was approximately 150 m, and the total time of pumping priming was about 75 min. It can be calculated from this that the length of pumping priming was 2 m/min, the time of the sand-carrying fluid stage was 2 min, the diameter of the proppant support column was approximately 5 mm, and the height of fracture was approximately 5 mm. The minimum horizontal principal stress of the reservoir was 50 MPa, the elasticity modulus was 30 GPa, and Poisson's ratio was 0.28. Taking the height of the proppant column as 5 mm, the diameter as 5 m, and the distance as 5 m for the calculation, the parameters required for numerical simulation can be obtained. This article assumes that the support column is tightly bonded together by fibers and ignores the shedding of proppant particles outside the support column during the fracturing process.

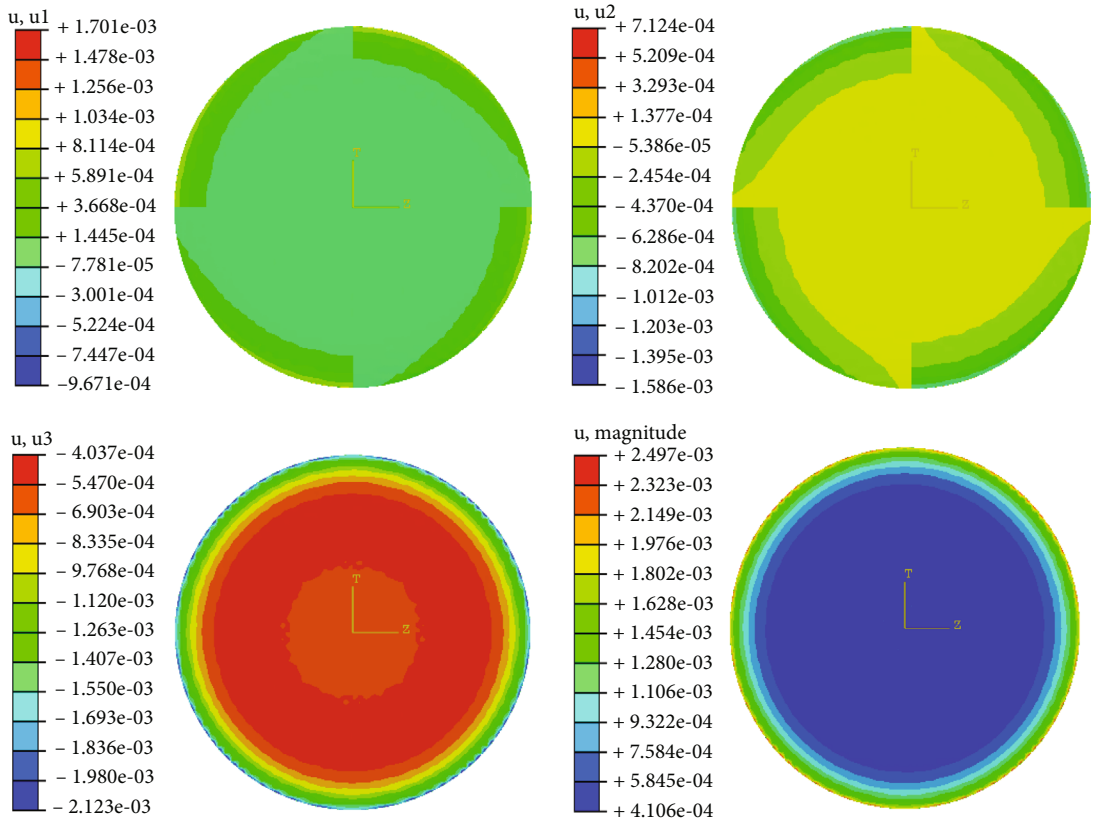

Figure 14: Displacement cloud images of proppant column.

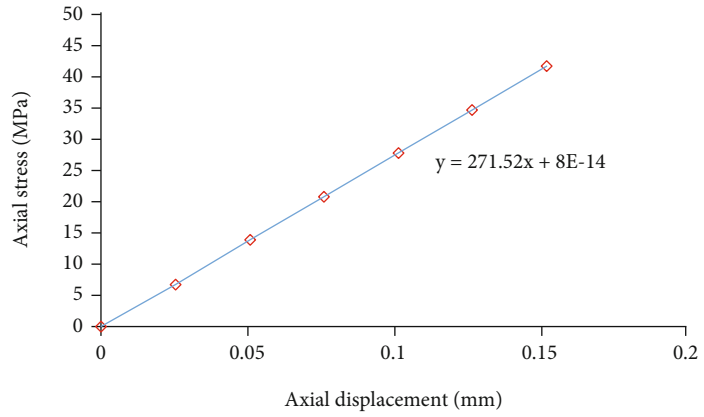

Figure 15: Halliburton laboratory experimental data [1].

3.1.2. Finite Element Model of Fracturing Crack-Proppant Column Interaction in High-Conductivity Channel. The global size of our finite element model was set at 0.1 m (Figure 11). With partitioning technology of swept mesh entities, the proppant column used hexahedron elements and a global size of 0.025 m. The top and bottom rock plates were subjected to the same closure stress, which were 40 MPa, 50 MPa, and 60 MPa one after another. The upper and lower rock slabs were set as surface-to-surface contact, ignoring the friction generated when the upper and lower rock plates are in contact; the normal direction was set as hard contact, and the scaling factor of hardness is set as 1. Although in the actual postcompression conditions the proppant particles may be broken under high closing pressure, we have not taken into account this effect in our simulations. The reason is that this study is conducted for tight oil reservoirs in the Shengli oilfields, China, and the fracture closure pressure ranges from 40 to 60 MPa whereas the selected proppant breakage pressure is 70 MPa. Thus, it is expected that proppant breakage may not occur.

3.2. Analysis of the Simulation Results of Fracturing Crack-Proppant Column Interaction in High-Conductivity Channel. Based on the finite element model of fracturing

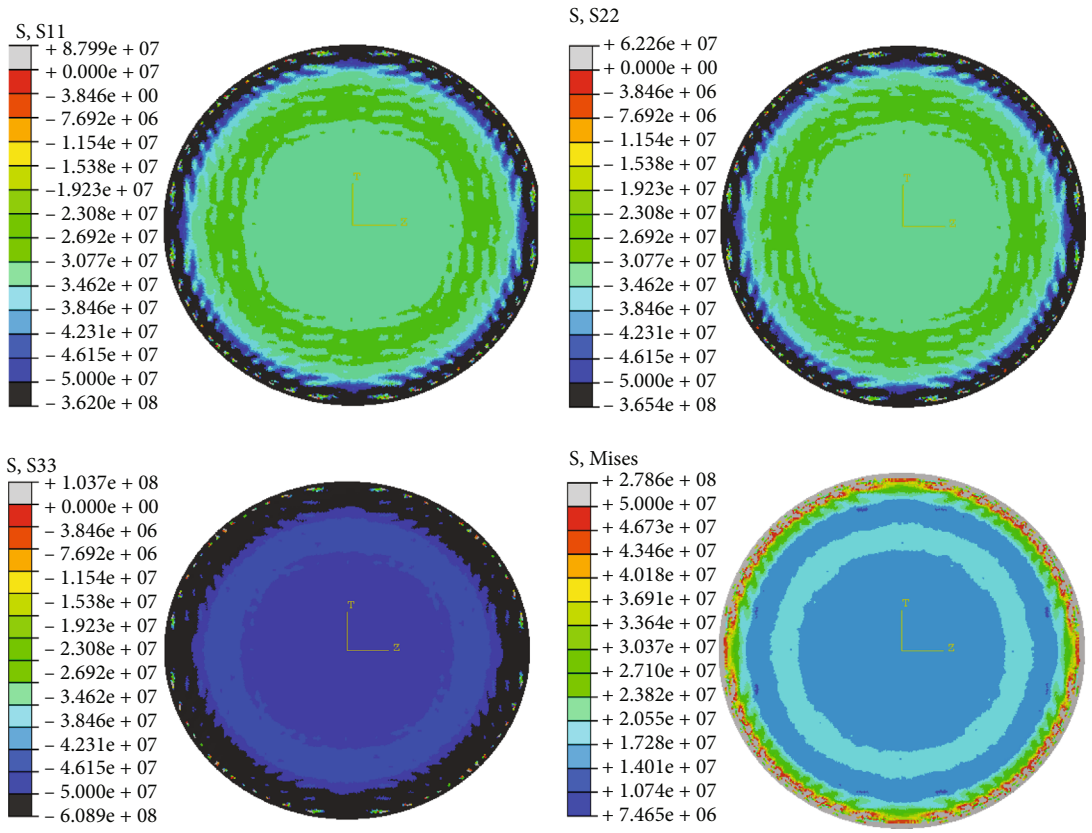

Figure 16: Displacement stress cloud images of proppant column.

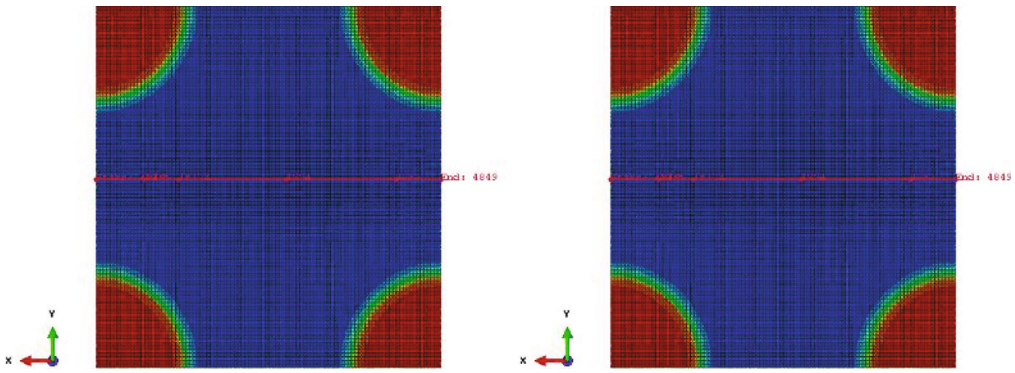

Figure 17: Schematic diagram of path.

crack-proppant column established in the previous section, this section simulated the interaction process and obtained the characteristics of the displacement and contact stress of the upper and lower rock plates and the displacement and stress of the proppant column.

As can be seen from Figure 12, the displacement of the center position of the upper slab in the negative direction along the Z direction is 6.175 mm, and the displacement of the center position of the lower slab in the negative direction along the Z direction is 0.6675 mm, so the relative displacement of the upper and lower slabs is 5.5075 mm. Since the total height of the proppant column is 5 mm, the upper and lower slabs have been in contact, and the proppant column cannot effectively support the fracture.

As can be seen from Figure 13, the contact stress on the outside of the proppant column and the center of the plate is greater than 50 MPa, while the contact stress on the other parts is slightly less than 50 MPa. This indicates that although the fracture is closed, the contact stress in some areas of the fracture is still less than the closure stress of the reservoir. According to the conventional conductivity experiment and theoretical study in the continuous sanding chamber, it is known that the decrease of the fracture closure stress can significantly improve the conductivity of the

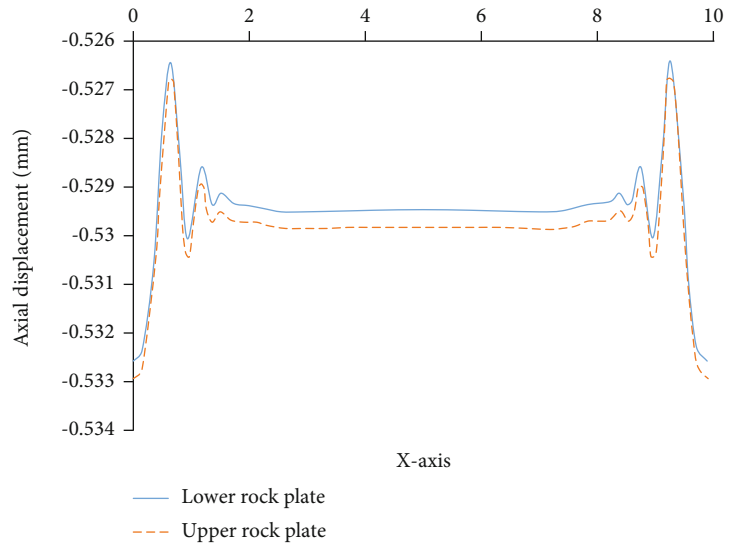

Figure 18: Axial displacement curve of upper and lower slabs.

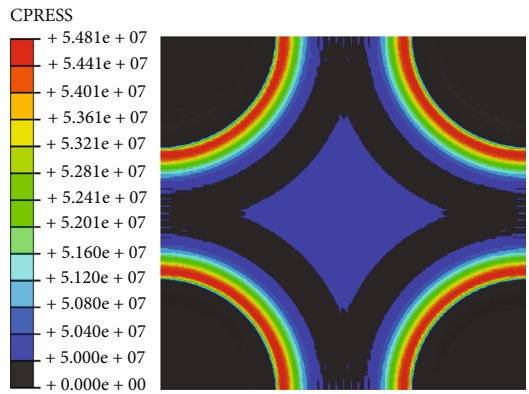

Figure 19: Contact stress nephogram of rock plate.

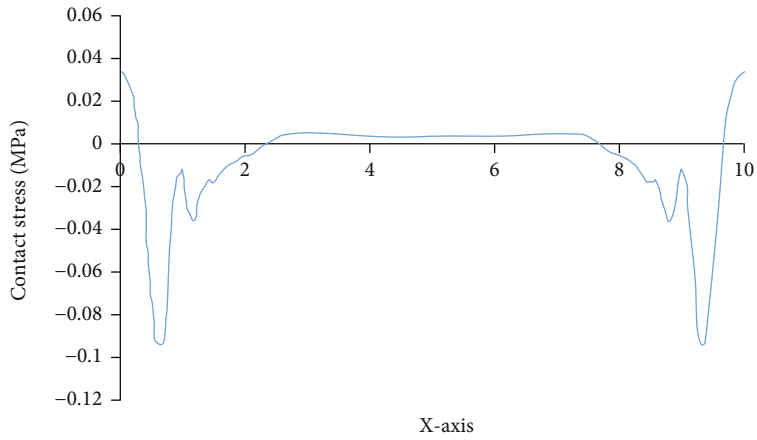

Figure 20: Contact stress curve of rock plate.

fracture, and the proppant column can still play a certain role in improving the conductivity of the fracture.

As shown in Figure 14, under the action of a closing stress of 50 MPa, the axial displacement of the proppant column is 0.21 mm, and the radial displacement in the X and Y directions is 1.7 mm and 1.58 mm, respectively. According to the results of the laboratory slab compression experiment of the proppant column (as shown in Figure 15), the axial

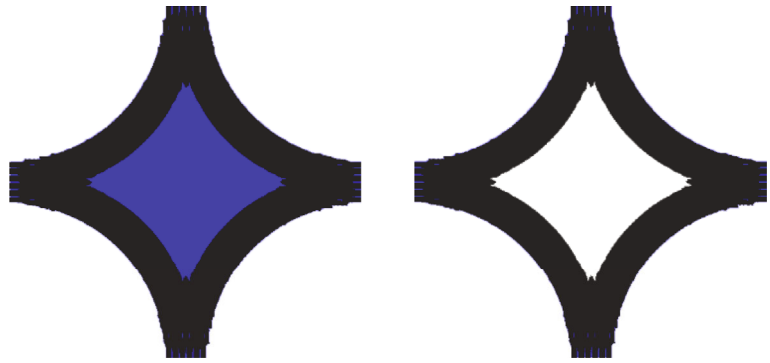

Figure 21: Total fracture area and effectively propped fracture zone.

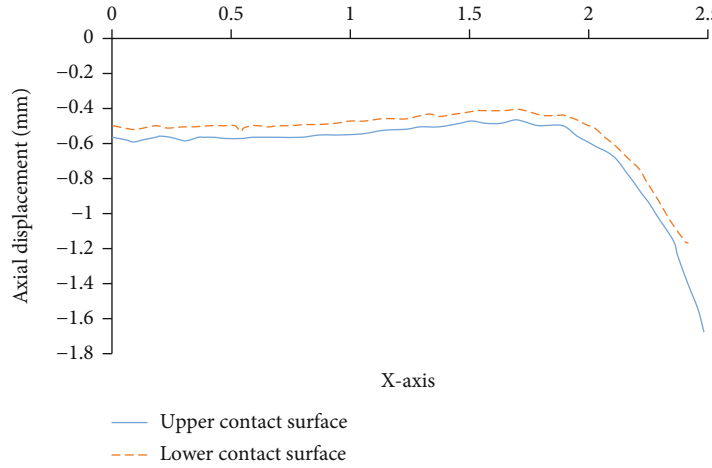

Figure 22: Axial displacement of proppant contact surfaces.

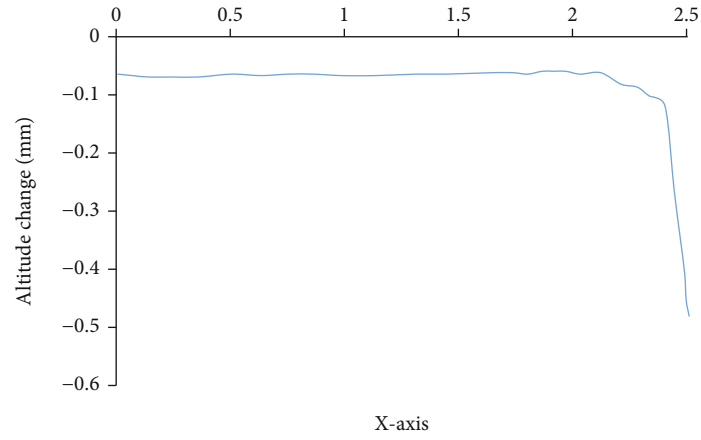

Figure 23: Height variation of proppant column.

displacement of the proppant column is about 0.18 mm under the condition of a closing stress of 50 MPa. The numerical simulation results are in good agreement with the experimental results, which indicates that the numerical simulation results have good reliability.

As can be seen from Figure 16, due to its large displacement and large normal stress, the outer ledge of the proppant column is prone to compressive stress failure under the action of the 50 MPa closing stress. Meanwhile, the local edge is also accompanied by the tensile stress failure, so the proppant column is prone to edge peeling and peripheral diffusion during compression.

3.2.1. Propping Characteristics of High-Conductivity Channel-Fracturing Fracture. In order to study whether the fractures in the middle of the proppant column are closed after

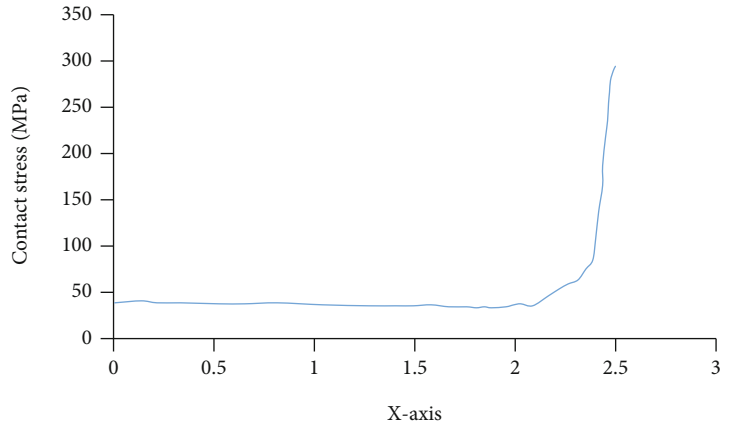

Figure 24: Contact stress of proppant interface.

Table 4: Detdetailed parameters of numerical simulation calculation of high-conductivity channel fracturing.

Factors	Value			
Diameter of proppant column (m)	1	3	5	—
Height of proppant column (mm)	2	5	8	—
Crustal stress (MPa)	40	50	60	—
Elastic modulus of the formation (GPa)	25	30	35	40

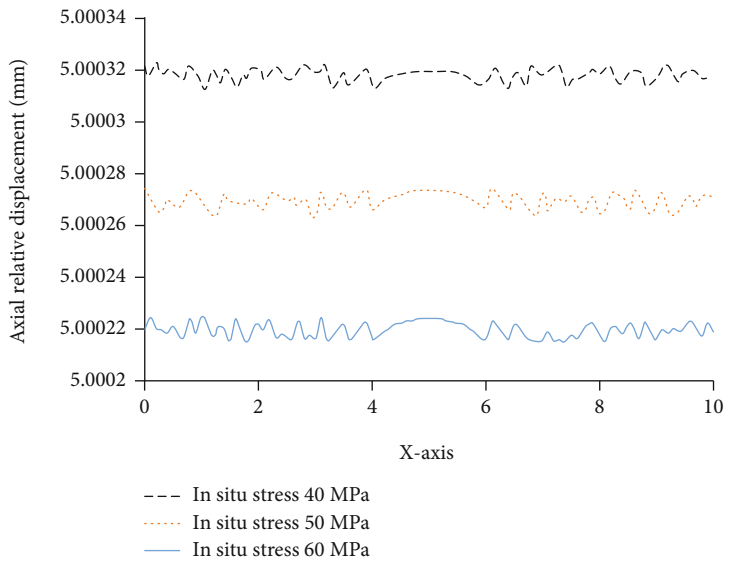

Figure 25: Relative axial displacement diagram of two rock slabs under different crustal stresses (elastic modulus 40 GPa).

fracturing fluid flowback in the high-conductivity channel fracturing and the value of the contact stress after closure, a path is set in the middle of the model along the X and Y directions (as shown in Figure 17), so as to plot the mutual displacement and contact stress of the left and right fracture walls.

Since the model has the same proppant column size and spacing, only the X direction calculation results are analyzed according to the symmetry principle.

In the axial displacement curve, the contact surface of the lower rock plate is set as the X-axis. Under the action of closure stress, the axial displacements of the two rock plates are both negative. Subtracting the absolute value of the axial displacement of the upper rock plate by 5 mm is to form the comparison diagram as shown in Figure 18. Therefore, the distance between the upper and lower rock plates can be obtained by subtracting the axial displacement of the upper rock plate from the axial displacement of the lower rock plate. As can be seen from the figure, the distance between the two plates is negative, which indicates that the crack has been closed. The larger the negative value is, the

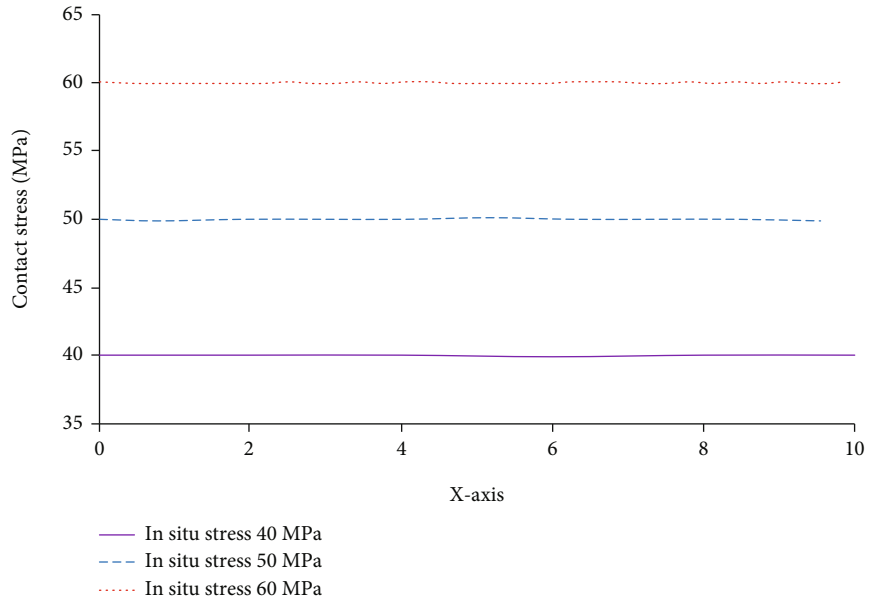

Figure 26: Comparison diagram of rock slab contact stress under different crustal stresses (elastic modulus 40 GPa).

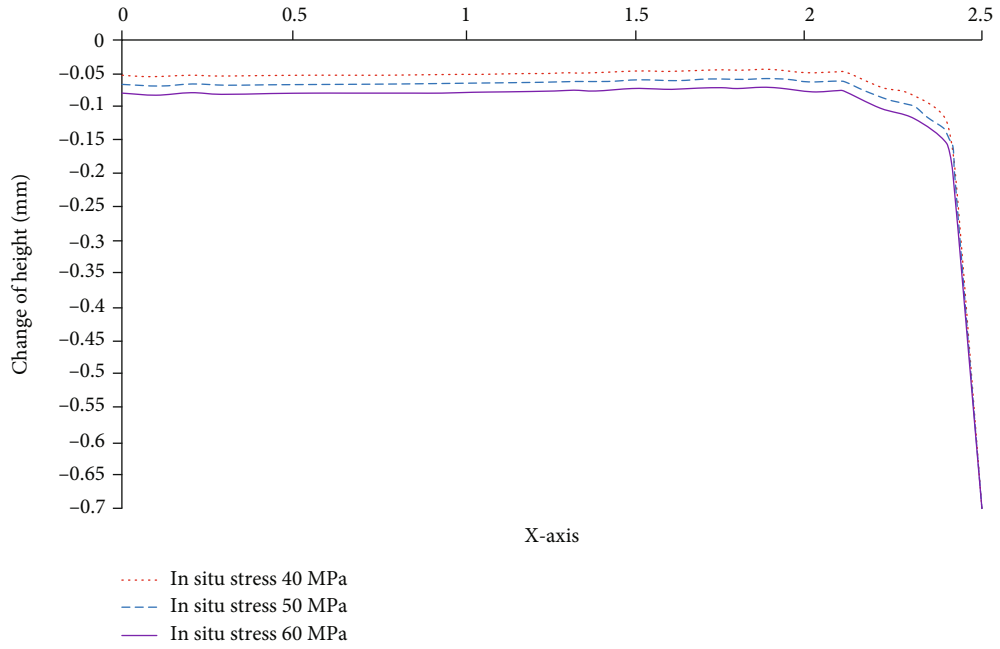

Figure 27: The change value of proppant height under different in situ stresses (elastic modulus 40 GPa).

more serious the compaction of the two plates will be. Compared with the two sides of the slab, the compaction degree in the middle part of the slab is more serious.

Figures 19 and 20 are the contact stress nephogram of the rock plate and the contact stress curve of the rock plate, respectively. In Figure 20, 50 MPa has been subtracted from the vertical coordinates, so the X-axis corresponds to the contact stress of 50 MPa. As can be seen from Figure 20, the contact stress at the center of the rock plate is greater than 50 MPa, while the contact stress at some parts of both ends is less than 50 MPa. The initial crustal stress is 50 MPa, which means that although the fracture is closed after that the proppant column is added, the closure stress in some areas of the fracture decreases, which significantly improves the conductivity of the fracture.

In the contact stress of the rock plate, the proppant column was partially removed to obtain the area shown in Figure 21(a). In the total fracture area, the black part is the area where the closure stress is less than 50 MPa, which is called the effective propping fracture area, as

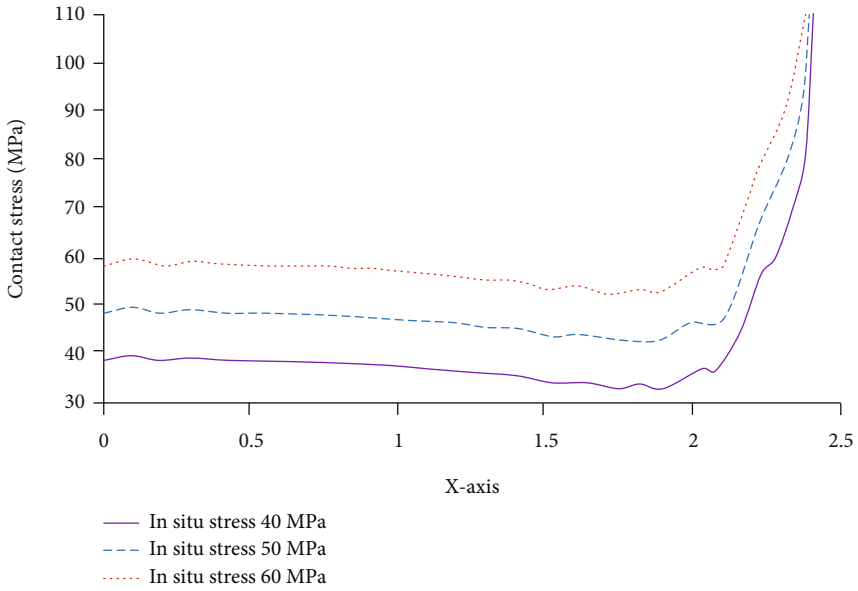

Figure 28: Comparison of contact stress of proppant under different in situ stresses (elastic modulus 40GPa).

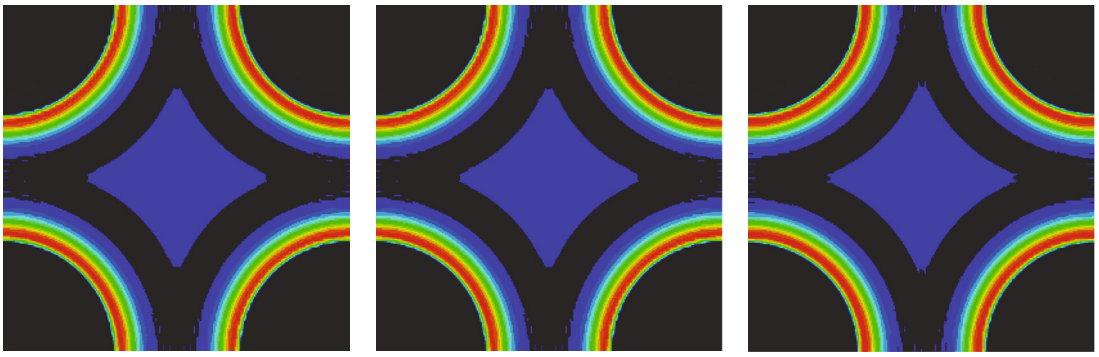

(a) 40 MPa (b) 50 MPa (c) 60 MPa

Figure 29: Contact stress cloud diagram of rock slab under different in situ stresses.

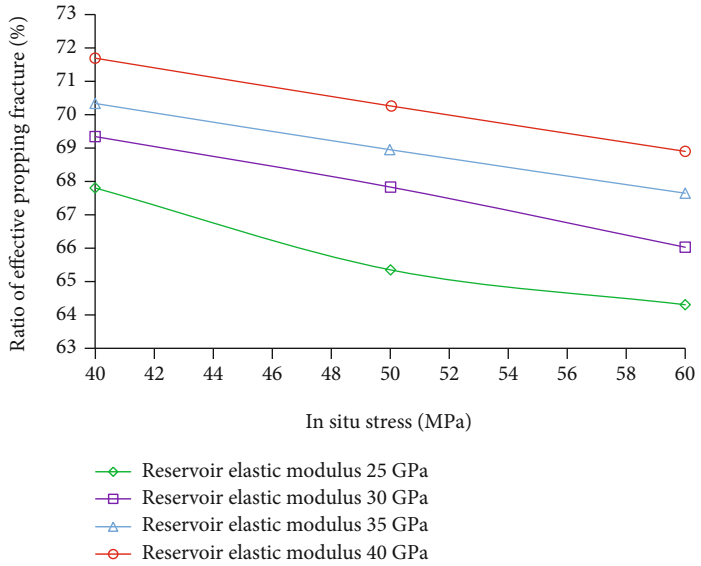

Figure 30: The influence of in situ stress on effective supporting cracks.

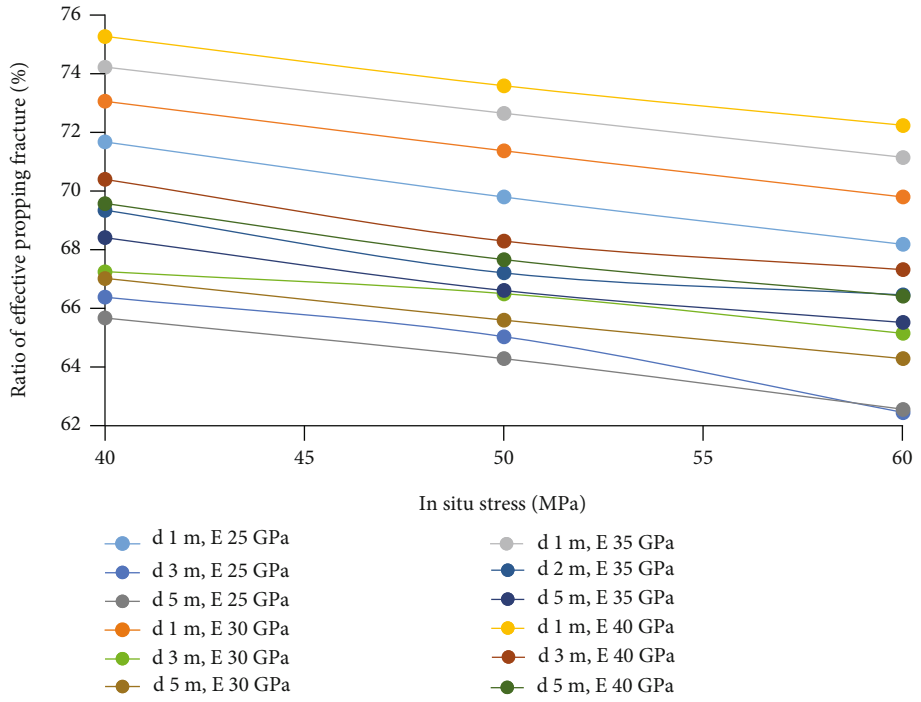

Figure 31: The proppant height is 3 mm, and the influence of in situ stress under different diameters on the ratio of effective supporting fractures.

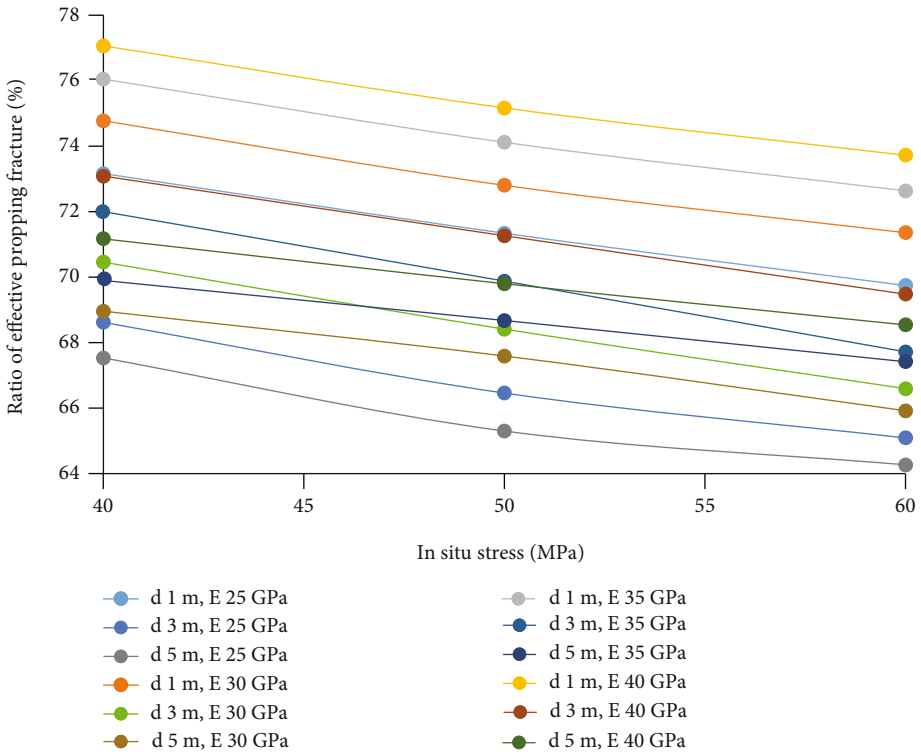

Figure 32: The proppant height is 5 mm, and the influence of in situ stress under different diameters on the ratio of effective supporting fractures.

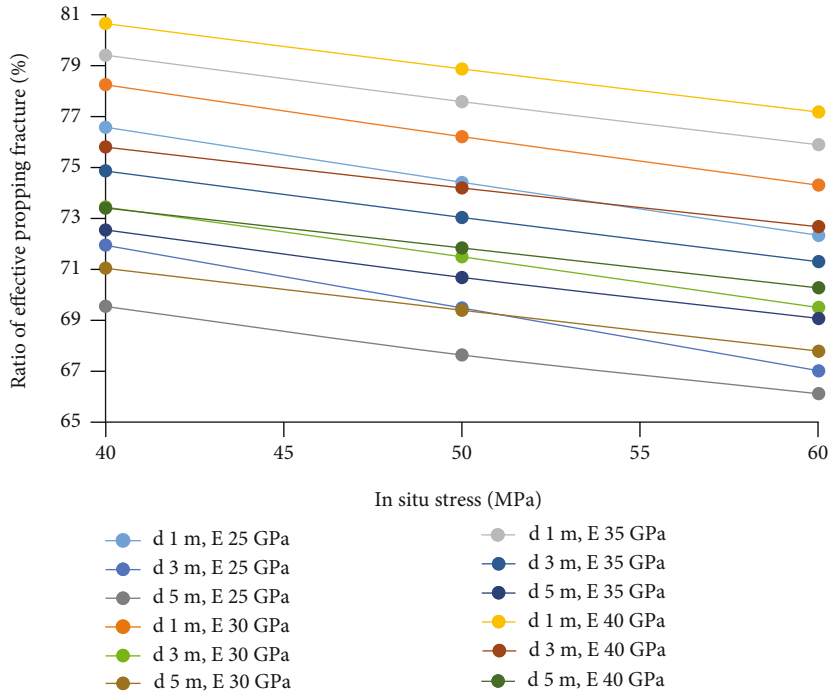

Figure 33: The proppant height is 8 mm, and the influence of in situ stress under different diameters on the ratio of effective supporting fractures.

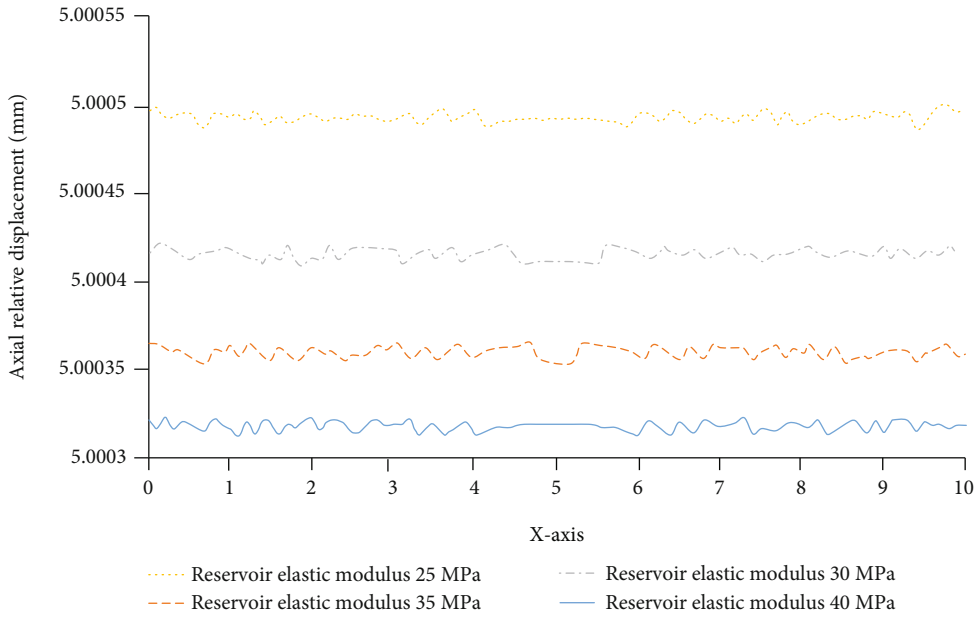

Figure 34: Axial relative displacement of two rock slabs under different reservoir elastic moduli (60 MPa in situ stress).

shown in Figure 21(b). Set the total fracture area as A and the area of the effectively supported fracture area calculated by the graphic analysis software as B. Assuming that the total fracture area is A, the area of the effective propping fracture area calculated by the graphic analysis software is B. After calculation, $B/A = 0.678$, indicating that the proportion of the effective propped fractures is 67.8%.

On this basis, the displacement and deformation characteristics of the proppant column are further analyzed to explain the stress-strain form of the proppant column.

As can be seen from Figure 22, the axial displacement of the central part of the proppant column is relatively small, while the axial displacement of the edge of the proppant column is larger. The absolute value of the axial displacement

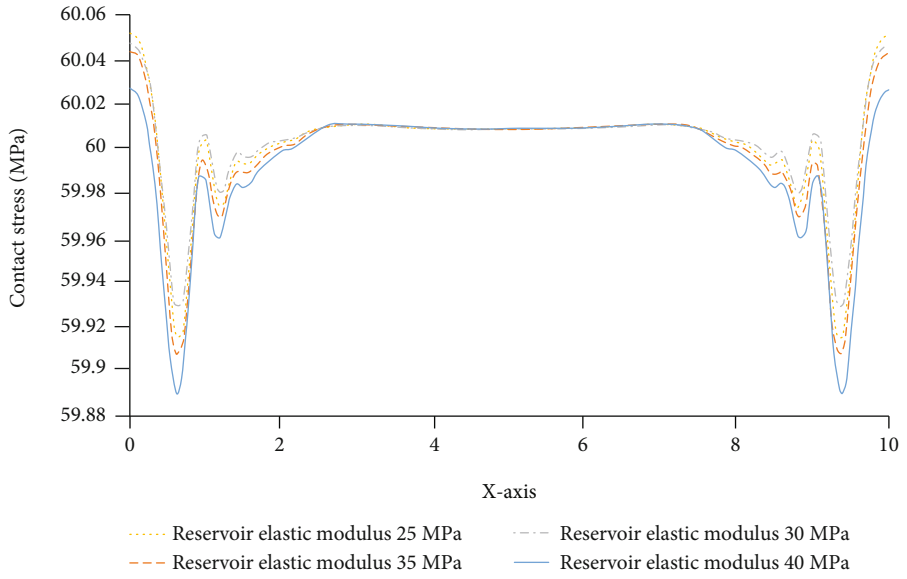

Figure 35: Comparison of contact stress of rock slab under different elastic moduli (in situ stress 60 MPa).

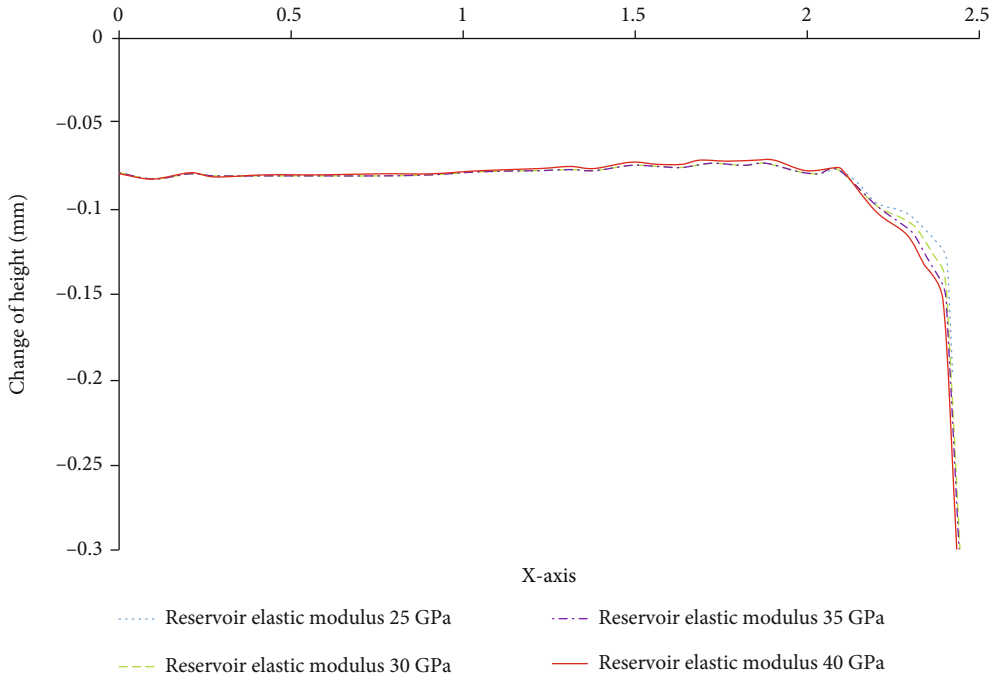

Figure 36: The height change of proppant under different elastic moduli (in situ stress 60 MPa).

of the upper contact surface is greater than that of the lower contact surface, so the height of the proppant column decreases. Figure 23 shows the compression of different parts of the proppant column. What is seen from the figure is that the height of the edge part of the proppant column decreases significantly.

The force distribution between the two contact surfaces of the proppant column is basically the same. As we can see from Figure 24, the contact stress is the largest at the edge of the proppant column, so compressive stress failure is more likely to occur and the proppant column is more prone to edge peeling and peripheral diffusion during compression.

4. Closure Deformation and Stability of Highly Conductive Fracture Channels and Proppant Columns

The crustal stress of the reservoir in the B oilfield is 40~60 MPa, the elastic modulus is 25~40 GPa, and Poisson's ratio is 0.27~0.28, which are in line with the geological

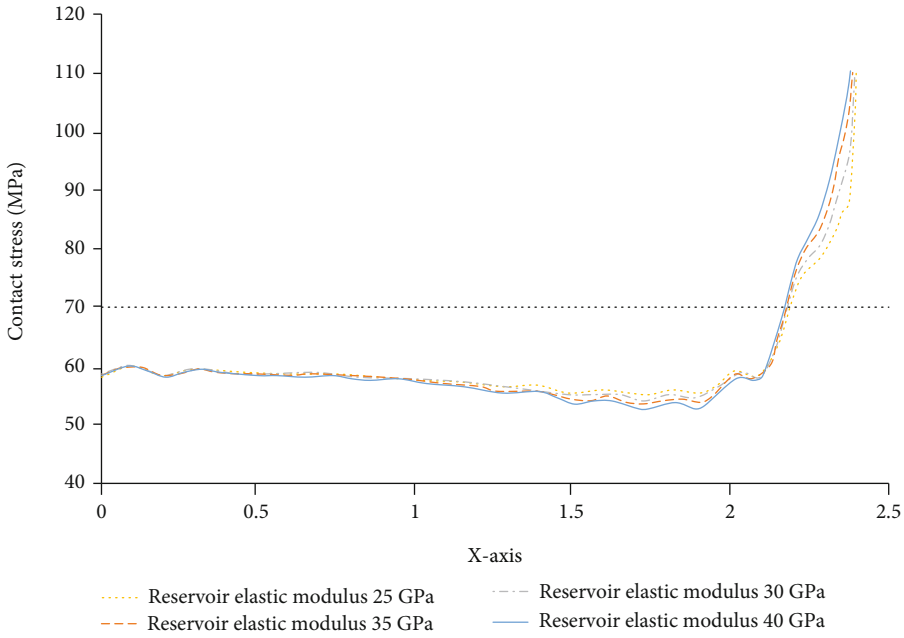

Figure 37: Contact stress of proppant under different elastic moduli (in situ stress 60 MPa).

Figure 38: Contact stress cloud diagram of rock slab under different reservoir elastic moduli (25 GPa, 30 GPa, 35 GPa, and 40 GPa).

conditions of high-conductivity channel fracturing. The heights of the proppant columns were 3 mm, 5 mm, and 8 mm. The diameters of the proppant columns were 1 m, 3 m, and 5 m, respectively. This means that the model sizes were 2 m, 6 m, and 10 m, respectively.

Now, the elastic modulus of the formation is set as 25 GPa, 30 GPa, 35 GPa, and 40 GPa, and Poisson's ratio is 0.28. The minimum horizontal principal stresses are 40 MPa, 50 MPa, and 60 MPa; the elastic modulus of the proppant column is 1.7 GPa and Poisson's ratio is 0.41. The heights of the proppant column are 3 mm, 5 mm, and 8 mm; the diameters of the proppant columns are 1 m, 3 m, and 5 m, respectively. This means that the sizes of the models are 10 m, 6 m, and 2 m, respectively. Under the above parameter setting conditions, a total of 108 sets of numerical simulation calculations are required, some parameters of which are shown in Table 4.

4.1. Influence of Crustal Stress on Fracture Closure Deformation and Stability. In the case of the elastic modulus of 40 GPa, a proppant column with the height of 5 mm and the diameter of 5 m was taken as an example to discuss the effect of crustal stress on fracture closure deformation and stability.

4.1.1. Influence of Crustal Stress on Fracture Closure Deformation

(1) Displacement Correlation of Two Fracture Planes. As can be seen from Figure 25, with the increase of crustal stress, the relative axial displacement of the two rock slabs also increases, and the two rock slabs are compressed more closely. The relative axial displacements of the two rock plates under each pressure are greater than 5 mm, which indicates that the fracture has been closed.

(2) Contact Stress Correlation of Two Fracture Planes. The upper and lower slabs are in contact with each other, so the contact stresses on the upper and lower surfaces are the same. It can be seen from Figure 26 that, with the increase of the crustal stress, the contact stress on the rock plate gradually increases, making it more prone to deformation and breakage.

4.1.2. The Influence of In Situ Stress on the Stability of Fracture-Proppant. It can be seen from Figure 27 that the height change value of the proppant also increases with the increase of the in situ stress. From the contact stress shown in Figure 28, it can be seen that the contact stress of the proppant increases with the increase of the in situ stress.

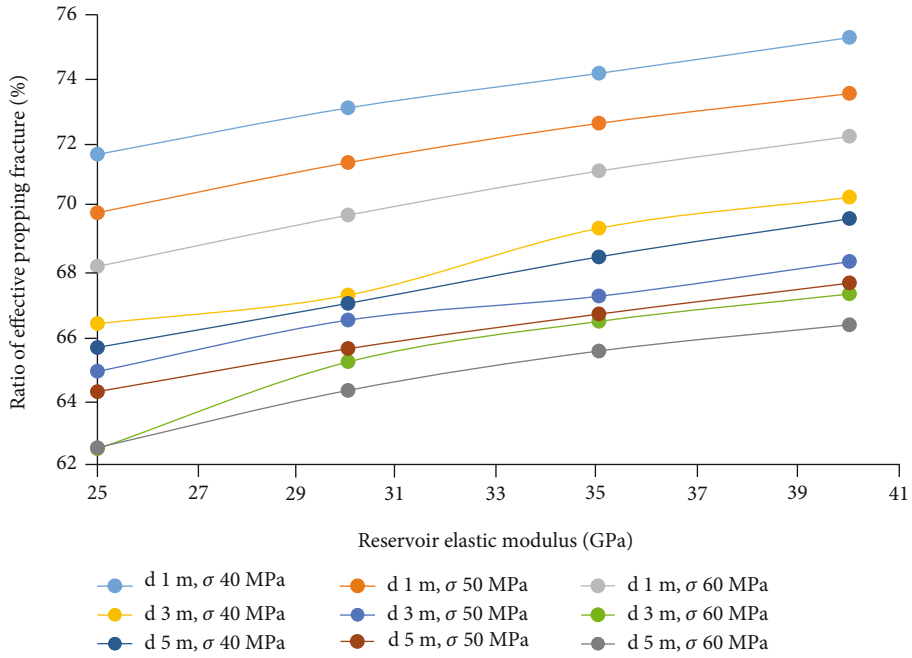

Figure 39: The influence of reservoir elastic modulus at 3 mm height and different diameters on the ratio of effective supporting fractures.

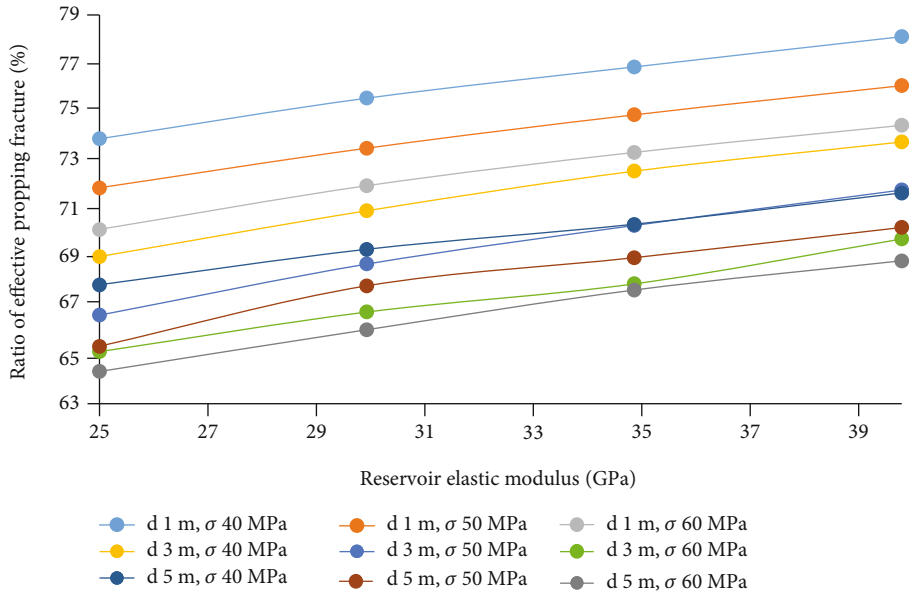

Figure 40: The influence of reservoir elastic modulus at 5 mm height and different diameters on the ratio of effective supporting fractures.

The greater the in situ stress, the larger the change of the proppant height, diameter, and contact stress.

4.1.3. The Influence of Reservoir Elastic Modulus on the Stability of Fracture-Proppant

(1) Proportion of Effective Supporting Cracks (Taking a Proppant with a Height of 5 mm and a Diameter of 5 m as an Example). As shown in Figure 29, from left to right, the contact stress cloud diagrams of rock slabs under in situ stress of 40 MPa, 50 MPa, and 60 MPa (elastic modulus 40 GPa) are shown. Using graphic analysis software, it is possible to calculate the proportion of effective supporting cracks under various stresses: 40 MPa is 71.69%, 50 MPa is 70.26%, and 60 MPa is 68.9%. Figure 30 shows that when the elastic modulus of the reservoir remains unchanged, as the in situ stress increases, the effective support ratio of the fracture decreases.

(2) The Influence of In Situ Stress on Effective Supporting Cracks under Different Height-to-Diameter Ratios. According to Figures 31–33, the simulation results show that when the elastic modulus is constant, the effective support ratio decreases with

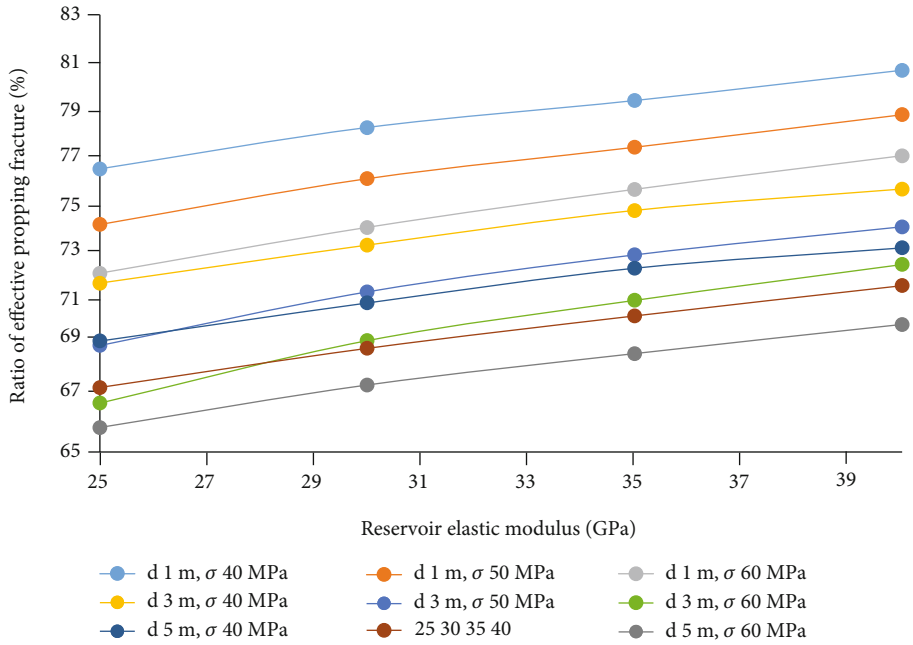

Figure 41: The influence of reservoir elastic modulus at 8 mm height and different diameters on the ratio of effective supporting fractures.

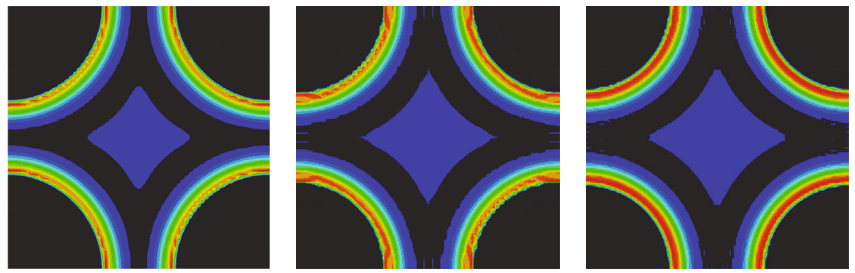

(a) Diameter of proppant 1 m (b) Diameter of proppant 3 m (c) Diameter of proppant 5 m

Figure 42: Contact stress cloud diagram of rock slab under different proppant diameters.

the increase of the in situ stress, and the reservoir elastic modulus has a greater influence on the effective support ratio.

4.2. Influence of Reservoir Elastic Modulus on Fracture Closure Deformation and Stability. When the in situ stress is 60 MPa, a proppant with a height of 5 mm and a diameter of 5 m is taken as an example to explore the influence of the reservoir elastic modulus on fracture closure deformation and stability.

4.2.1. Influence of Reservoir Elastic Modulus on Fracture Closure Deformation

(1) The Relationship between the Displacements of the Upper and Lower Fracture Surfaces. It can be seen from Figure 34 that under the condition of constant in situ stress, as the elastic modulus of the reservoir increases, the relative axial displacement of the upper and lower rock slabs gradually decreases.

(2) The Relationship between the Contact Stresses of the Upper and Lower Cracks. It can be seen from Figure 35 that under the condition of a constant in situ stress, as the elastic modulus of the reservoir increases, the contact stress on the part of the rock slab with a contact stress of less than 60 MPa gradually decreases, and the central parts of the rock slab are basically the same, but the slabs change irregularly on both sides.

4.2.2. The Influence of Reservoir Elastic Modulus on the Stability of Fracture-Proppant. It can be seen from Figure 36 that under the condition of a constant in situ stress, the decrease in the height of the edge of the proppant increases as the elastic modulus of the reservoir increases, while the remaining part decreases.

It can be seen from Figure 37 that under the condition of a constant in situ stress, the contact stress at the edge of the proppant increases as the elastic modulus of the reservoir increases, while the remaining part decreases.

Under the condition of the constant in situ stress, after the elastic modulus of the reservoir changes, no matter the height or contact stress, the change is very small. Therefore,

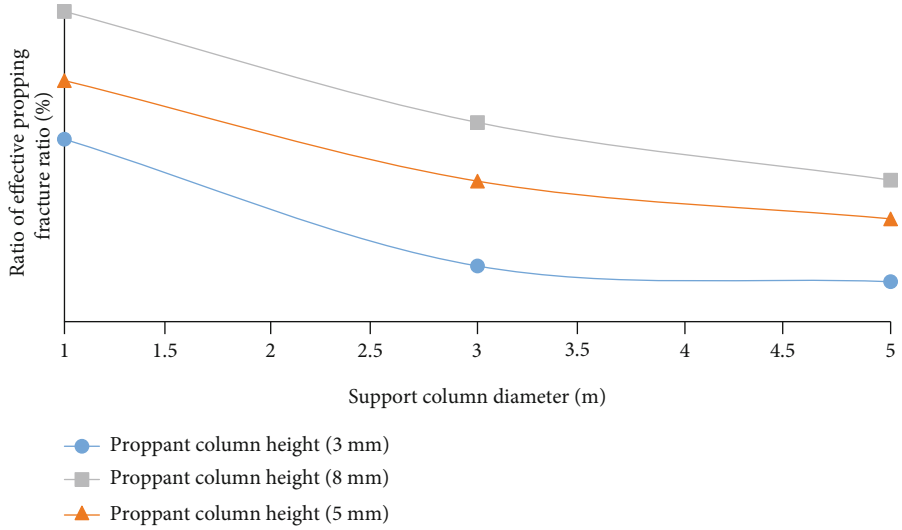

Figure 43: The effect of proppant diameter on effective supporting fractures.

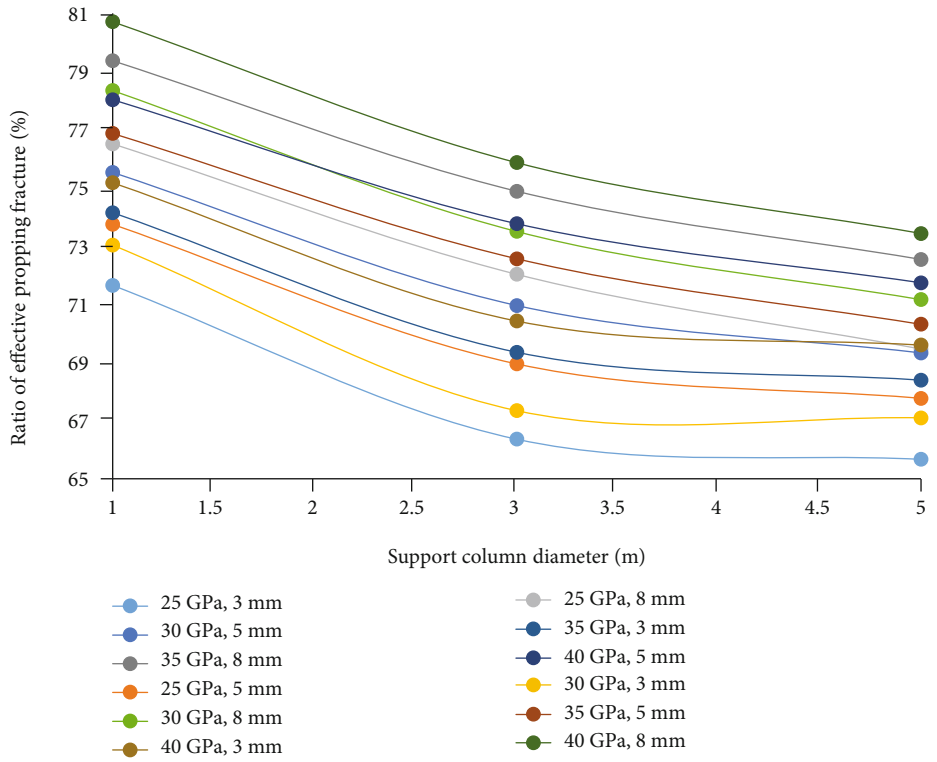

Figure 44: The effect of proppant diameter on the ratio of effective supporting fractures (in situ stress 40 MPa).

it can be concluded that the elastic modulus of the reservoir has little effect on the stability of the proppant.

As shown in Figure 38, from left to right, the contact stress cloud diagrams of the rock slab under the in situ stress of 25 GPa, 30 GPa, 35 GPa, and 40 GPa (elastic modulus 60 MPa) are shown. Using graphic analysis software, the proportion of effective supporting fractures under each reservoir elastic modulus can be calculated: 25 GPa is 64.32%, 30 GPa is 66.05%, 35 GPa is 67.64%, and 40 GPa is 68.90%. This shows that under the condition of a constant in situ stress, as the elastic modulus of the reservoir increases, the effective support ratio of fractures increases.

(1) Influence of Reservoir Elastic Modulus on Effective Supporting Fractures with Different Height-to-Diameter Ratios. According to Figures 39–41, the simulation results show that the ratio of effective supporting fractures increases with the increase of the elastic modulus of the reservoir,

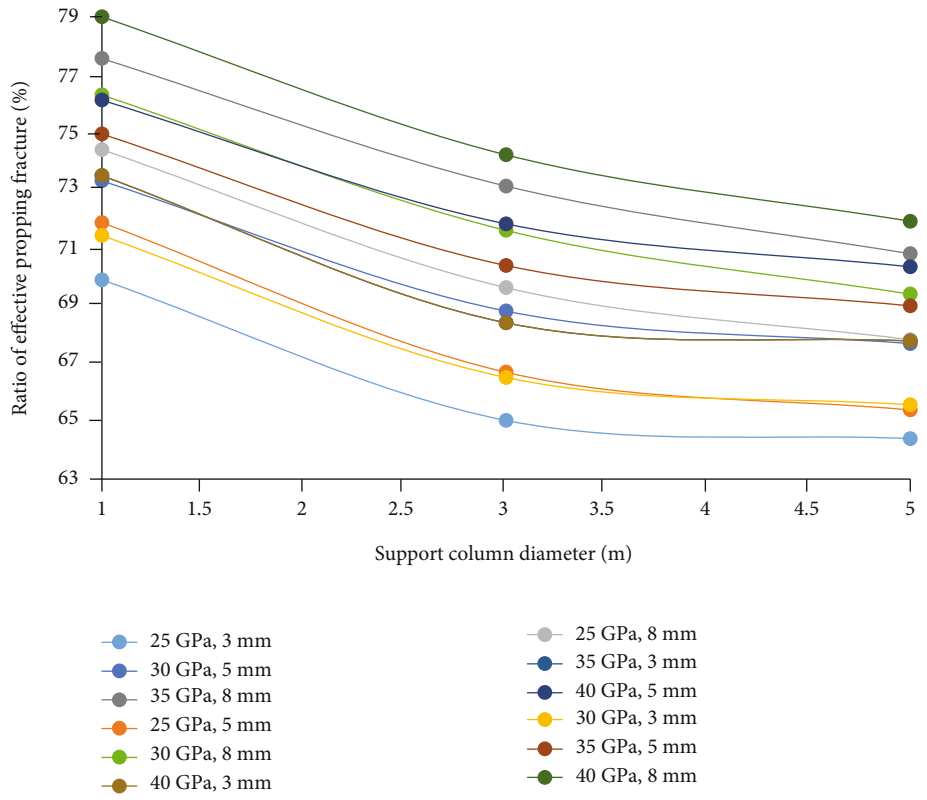

Figure 45: The effect of proppant diameter on the ratio of effective supporting fractures (in situ stress 50 MPa).

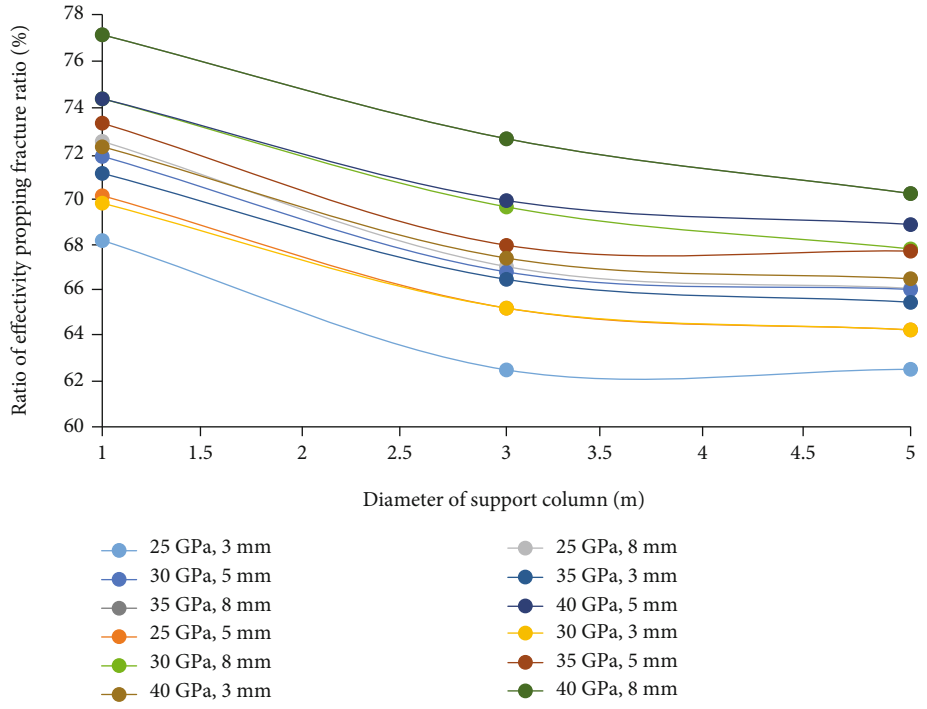

Figure 46: The influence of proppant diameter on the ratio of effective supporting fractures (in situ stress 60 MPa).

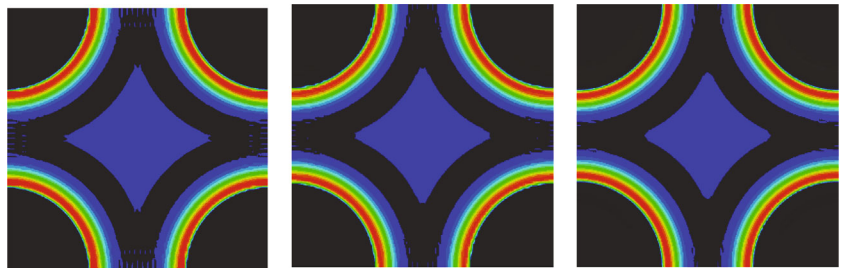

Figure 47: Contact stress cloud diagram of rock slab under different proppant heights (3 mm, 5 mm, and 8 mm).

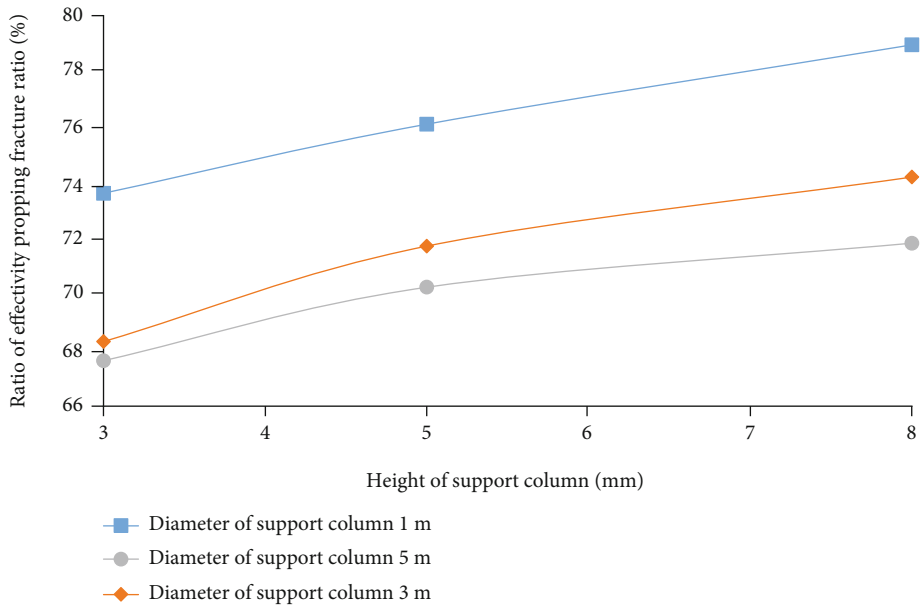

Figure 48: The effect of proppant height on effective supporting fractures.

and this increasing trend is not affected by the in situ stress.

4.3. The Influence of Proppant Diameter (Spacing) on Fracture Closure Deformation and Stability. When the height of the proppant is 5 mm, the in situ stress is set to 50 MPa and the elastic modulus of the reservoir is 40 GPa. The effect of the proppant diameter on fracture closure deformation and stability is explored.

4.3.1. Ratio of Effective Supporting Cracks. As shown in Figure 42, from left to right, the contact stress cloud diagrams of the rock slab when the proppant diameter is 1 m, 3 m, and 5 m (the height of the proppant is 5 mm) are shown. Using graphic analysis software, the proportion of effective supporting fractures under each proppant diameter can be calculated: 1 m is 76.02%, 3 m is 71.76%, and 5 m is 70.26%. Figure 43 shows that when the proppant height remains the same, as the diameter of the proppant increases, the effective support ratio of the fracture decreases.

4.3.2. The Effect of Proppant Diameter on Effective Supporting Fractures under Different In Situ Stresses and Elastic Moduli. When the in situ stress is 40 MPa, 50 MPa, and 60 MPa, and the elastic modulus is 25 GPa, 30 GPa, 35 GPa, and 40 GPa, the influence of the proppant diameter under the elastic modulus on the effective support fracture is shown in Figures 44–46.

According to the above simulation results, it can be seen that the ratio of effective proppant fractures decreases with the increase of the proppant diameter, and this decreasing trend is not affected by the height of the proppant. When the diameter of the proppant is 5 m, the in situ stress is set to 50 MPa, and the elastic modulus of the reservoir is 40 GPa. The effect of the proppant height on fracture closure deformation and stability is explored.

(1) Ratio of Effective Supporting Cracks. As shown in Figure 47, from left to right, the contact stress cloud diagrams of the rock slab when the proppant height is 3 mm, 5 mm, and 8 mm (proppant diameter 5 m) are shown. Using graphic analysis software, the proportion of effective supporting cracks under each proppant column height can be calculated: 3 mm is 67.68%, 5 mm is 70.26%, and 8 mm is 71.86%. Figure 48 shows that when the diameter of the

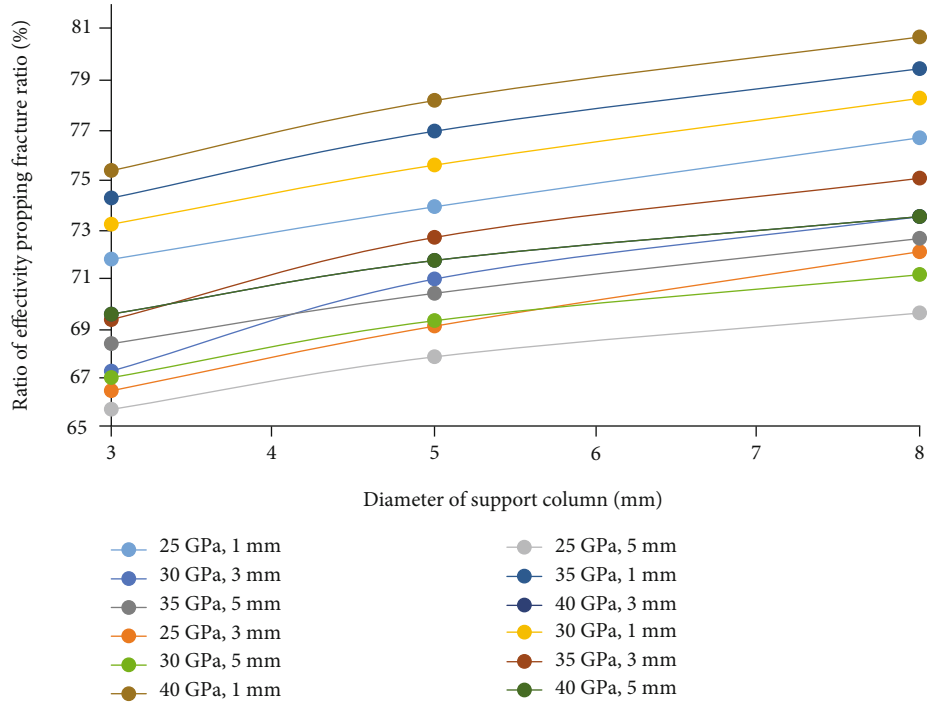

Figure 49: The effect of proppant height on the ratio of effective propped fractures under 40 MPa in situ stress and different elastic moduli.

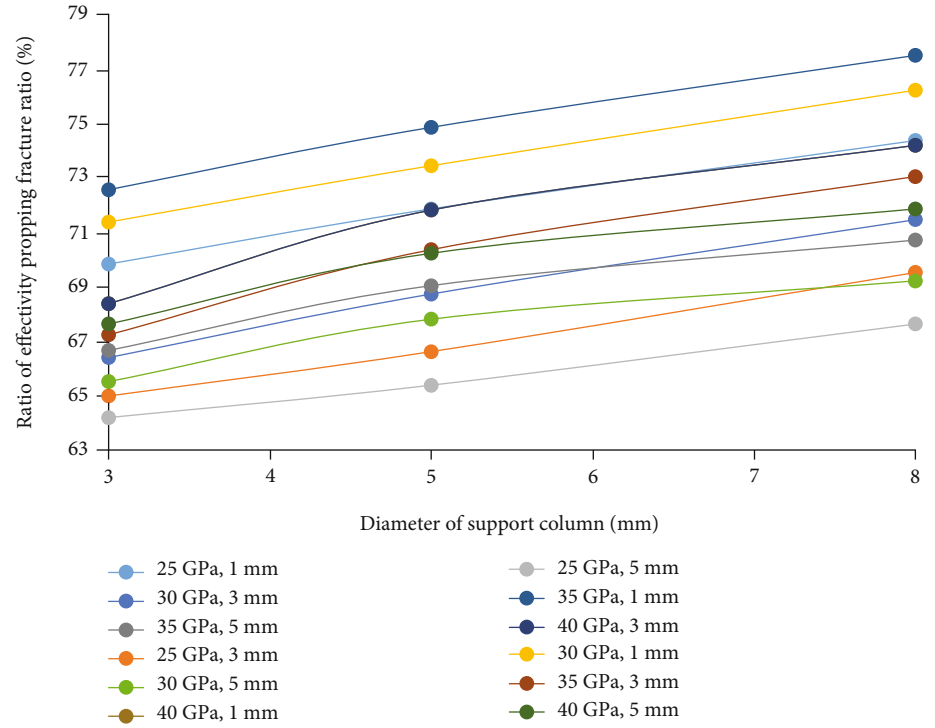

Figure 50: The effect of proppant height on the ratio of effective propped fractures under 50 MPa in situ stress and different elastic moduli.

proppant remains unchanged, as the height of the proppant increases, the effective support ratio of the fracture increases.

(2) The Effect of Proppant Height on Effective Supporting Fractures under Different In Situ Stresses and Elastic Moduli. According to the above simulation results (Figures 49–51), it can be seen that the ratio of effective supporting fractures increases with the height of the proppant column, and this increasing trend is not affected by the diameter of the proppant column.

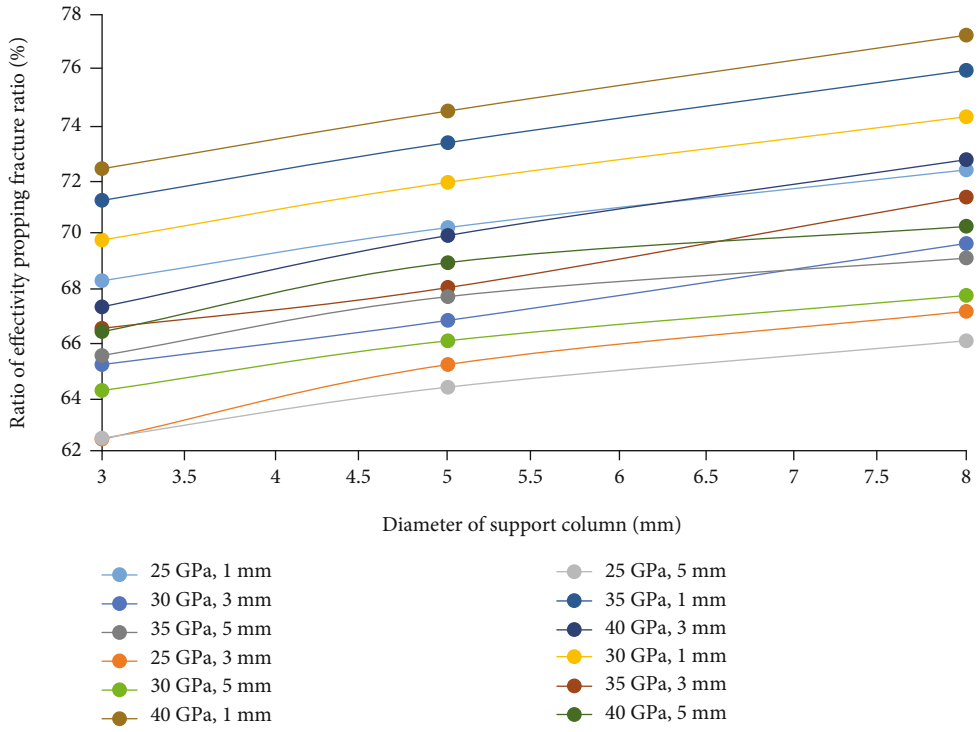

Figure 51: The effect of proppant height on the ratio of effective propped fractures under 60 MPa in situ stress and different elastic moduli.

5. Conclusion

This paper studies the influence of in situ stress, reservoir rock elastic parameters, and spatial distribution characteristics of proppant on the closed deformation of high-conductivity fracturing channels and the stability of the proppant. The main conclusions are as follows:

(1) The proppant particles have a large pore space in the low pressure section. As the pressure increases, the particles are compressed and tightly arranged. The axial and radial deformations of the proppant increase rapidly at the beginning of loading, and the strain changes slowly under high stress

(2) The greater the in situ stress, the greater the contact stress on the rock slab, the lower the height of the proppant, the larger the diameter, and the easier for the proppant to deform and break, while the effective support ratio decreases as the in situ stress increases

(3) Under the condition of constant in situ stress, as the elastic modulus of the reservoir increases, the relative axial displacement of the two rock slabs gradually decreases, and as the effective support ratio of the fracture increases, the impact of reservoir elastic modulus on the stability of proppant decreases

(4) The effective support ratio of fractures decreases with the increase of the proppant diameter, increases with the increase of the proppant height, and increases with the ratio of reservoir elastic modulus to in situ stress. When the proppant diameter (proppant spacing) is less than or equal to 3 m, the ratio of effective supporting fractures increases significantly

Data Availability

Data will be made available on request.

Conflicts of Interest

The authors declare that they have no conflicts of interest.

References

[1] M. Gillard, O. Medvedev, A. Peña, A. Medvedev, F. Peñacorada, and E. d'Huteau, "A new approach to generating fracture conductivity," in *SPE Annual Technical Conference and Exhibition*, Florence, Italy, September 2010.

[2] R. Kayumov, A. Klyubin, A. Yudin et al., "First channel fracturing applied in mature wells increases production from Talinskoe oilfield in Western Siberia," in *SPE Russian Oil and Gas Exploration and Production Technical Conference and Exhibition*, Moscow, Russia, October 2012.

[3] S. Wang, X. Wang, L. Bao, Q. Feng, X. Wang, and S. Xu, "Characterization of hydraulic fracture propagation in tight formations: a fractal perspective," *Journal of Petroleum Science and Engineering*, vol. 195, article 107871, 2020.

[4] L. Yang, C. Chen, Y. Liu, and Y. Zheng, "A comparative study of ion diffusion during water imbibition in shale, sandstone and volcanic rock," *Capillarity*, vol. 3, no. 2, pp. 16–27, 2020.

[5] S. Xu, Q. Feng, S. Wang, F. Javadpour, and Y. Li, "Optimization of multistage fractured horizontal well in tight oil based

on embedded discrete fracture model," *Computers & Chemical Engineering*, vol. 117, pp. 291–308, 2018.

[6] S. Wang, C. Qin, Q. Feng, F. Javadpour, and Z. Rui, "A framework for predicting the production performance of unconventional resources using deep learning," *Applied Energy*, vol. 295, article 117016, 2021.

[7] T. Guo, S. Wang, S. Liu, J. Xu, N. Qi, and Z. Rui, "Physical simulation of hydraulic fracturing of large-sized tight sandstone outcrops," *SPE Journal*, vol. 26, no. 1, pp. 372–393, 2021.

[8] Q. Feng, S. Xu, X. Xing, W. Zhang, and S. Wang, "Advances and challenges in shale oil development: a critical review," *Advances in Geo-Energy Research*, vol. 4, no. 4, pp. 406–418, 2020.

[9] Z. Rui, T. Guo, Q. Feng, Z. Qu, N. Qi, and F. Gong, "Influence of gravel on the propagation pattern of hydraulic fracture in the glutenite reservoir," *Journal of Petroleum Science and Engineering*, vol. 165, pp. 627–639, 2018.

[10] A. Valenzuela, J. Guzmán, S. Chávez et al., "Field development study: channel fracturing increases gas production and improves polymer recovery in Burgos Basin, Mexico North," in *SPE Hydraulic Fracturing Technology Conference*, The Woodlands, Texas, USA, February 2012.

[11] A. A. Gawad, J. Long, T. El-Khalek et al., "Novel combination of channel fracturing with rod-shaped proppant increases production in the Egyptian Western Desert," in *SPE European Formation Damage Conference & Exhibition*, Noordwijk, The Netherlands, June 2013.

[12] A. Q. Li, L. J. Mu, X. W. Li, Y. Haihua, T. Judd, and L. Yaolan, "The channel fracturing technique improves tight reservoir potential in the Ordos Basin," in *SPE/IATMI Asia Pacific Oil & Gas Conference and Exhibition*, Nusa Dua, Bali, Indonesia, October 2015.

[13] M. Meng, Z. Chen, X. Liao, J. Wang, and L. Shi, "A well-testing method for parameter evaluation of multiple fractured horizontal wells with non-uniform fractures in shale oil reservoirs," *Advances in Geo-Energy Research*, vol. 4, no. 2, pp. 187–198, 2020.

[14] Y. He, S. Cheng, Z. Sun, Z. Chai, and Z. Rui, "Improving oil recovery through fracture injection and production of multiple fractured horizontal wells," *Journal of Energy Resources Technology*, vol. 142, no. 5, article 053002, 2020.

[15] Z. Rui, K. Cui, X. Wang et al., "A quantitative framework for evaluating unconventional well development," *Journal of Petroleum Science and Engineering*, vol. 166, pp. 900–905, 2018.

[16] C. Li, H. Singh, and J. Cai, "Spontaneous imbibition in shale: a review of recent advances," *Capillarity*, vol. 2, no. 2, pp. 17–32, 2019.

[17] F. Guo, S. Wang, Q. Feng, X. Yao, Q. Xue, and X. Li, "Adsorption and absorption of supercritical methane within shale kerogen slit," *Journal of Molecular Liquids*, vol. 320, article 114364, 2020.

[18] Y. Heider, "A review on phase-field modeling of hydraulic fracturing," *Engineering Fracture Mechanics*, vol. 253, article 107881, 2021.

[19] P. D. Nguyen, L. K. Vo, C. Parton, J. Heeter, R. Gashimov, and P. O'Connell, "Evaluation of low-quality sand for proppant-free channel fracturing method," in *International Petroleum Technology Conference*, Malaysia, 2014.

[20] X. Yan, Z. Huang, X. Yan, J. Yao, Y. Li, and L. Gong, "Theoretical analysis of high flow conductivity of a fracture induced in HiWay fracturing," *Acta Physica Sinica*, vol. 64, no. 13, article 134703, 2015.

[21] X. Yan, Z. Huang, J. Yao, W. Song, Y. Li, and L. Gong, "Theoretical analysis of fracture conductivity created by the channel fracturing technique," *Journal of Natural Gas Science & Engineering*, vol. 31, pp. 320–330, 2016.

[22] T. Hou, S. Zhang, B. Yu et al., "Theoretical analysis and experimental research of channel fracturing in unconventional reservoir," in *SPE Europec Featured at Eage Conference and Exhibition*, Vienna, Austria, May 2016.

[23] G. Xu, S. Zhang, L. Wang, and J. Han, "Influence factors analysis of proppant fracture in channel fracturing," *Fault-Block Oil & Gas Field*, vol. 22, no. 4, pp. 534–537, 2015.

[24] Z. Qu, L. Zhou, G. Qu, D. Huang, Y. Yang, and H. Xu, "Experimental evaluation on influencing factors of flow conductivity for channel fracturing proppant," *Petroleum Geology and Recovery Efficiency*, vol. 22, no. 1, pp. 122–126, 2015.

[25] Q. Wen, Y. Yang, F. Wang, X. Duan, L. Yang, and Z. Jin, "Experimental study on an innovative proppant placement method for channel fracturing technique," *Journal of China University of Petroleum*, vol. 40, no. 5, pp. 112–117, 2016.

[26] J. C. Zhang, "Theoretical conductivity analysis of surface modification agent treated proppant," *Fuel*, vol. 134, pp. 166–170, 2014.

[27] J. C. Zhang and J. R. Hou, "Theoretical conductivity analysis of surface modification agent treated proppant II - channel fracturing application," *Fuel*, vol. 165, pp. 28–32, 2016.

[28] X. J. Zheng, M. Chen, B. Hou et al., "Effect of proppant distribution pattern on fracture conductivity and permeability in channel fracturing," *Journal of Petroleum Science and Engineering*, vol. 149, pp. 98–106, 2017.

[29] R. Moghadasi, A. Rostami, and A. Hemmati-Sarapardeh, "Application of nanofluids for treating fines migration during hydraulic fracturing: experimental study and mechanistic understanding," *Advances in Geo-Energy Research*, vol. 3, no. 2, pp. 198–206, 2019.

[30] J. C. Guo and Y. X. Liu, "Modeling of proppant embedment: elastic deformation and creep deformation," in *SPE International Production and Operations Conference & Exhibition*, Doha, Qatar, May 2012.

[31] B. R. Meyer, L. W. Bazan, D. E. Walls, and B. C. Brinzer, "Theoretical foundation and design formulae for channel and pillar type propped fractures – a method to increase fracture conductivity," in *SPE Annual Technical Conference and Exhibition*, Amsterdam, The Netherlands, October 2014.

[32] B. Hou, X. J. Zheng, M. Chen, Z. Ye, and D. Chen, "Parameter simulation and optimization in channel fracturing," *Journal of Natural Gas Science and Engineering*, vol. 35, pp. 122–130, 2016.